multiclimact

D9.1 - DEVELOPMENT OF FIBER OPTICS-BASED MONITORING SYSTEMS FOR FLOOD DEFENCES

D9.1 - Fiber optic-based monitoring systems for flood defence - development for the application towards the real demo

FEBRUARY 2026 | TUDELFT

MULTICLIMACT
D9.1 – FIBER OPTIC-BASED MONITORING SYSTEMS FOR FLOOD DEFENCE – DEVELOPMENT FOR THE APPLICATION TO A REAL DEMO

Project Title	MULTI-faceted CLIMate adaptation ACTions to improve resilience, preparedness and responsiveness of the built environment against multiple hazards at multiple scales
Project Acronym	MULTICLIMACT
Contract Number	101123538
Project Coordinator	Rina Consulting S.p.A.
WP Leader:	UNIVPM

Deliverable	D9.1 – Fiber optic-based monitoring systems for flood defence – development for the application to a real demo
DoA	T9.1 – Materials and technologies for improving the resilience at territorial level – development for the application to a real demo case
Lead beneficiary	TUDELFT
Main Authors	Juan Pablo Aguilar-López (TUDELFT)
Main contributors	Nils Nöther (Fibristerre) , Ilaria Ingrosso (RINA-C), Chimango Sanless Mweso (TU Delft), Sophia Luijendijk (DELFLAND), Juus Teensma (WL)
Reviewers	Michele Morici (UNICAM) Valeria Leggieri (UNICAM), Celina Solari (RINA-C), Alessandra Mobili (UNIVPM), Richard Kaculi (UNIVPM), Nibras Abo Alzahab (UNIVPM).
Due date	30.03.2026
Report date	25.03.2026
Version	V1.4

Document classification	PU Public

Co-funded by the European Union

REVISION TABLE

Version	Date	What
V1.0	01/01/2026	Table of Contents
V1.1	09/02/2026	First Draft
V1.2	16/02/2026	Draft after internal quality check
V1.3	01/03/2026	Document ready for quality control
V1.4	23/03/2026	Final version ready for submission

TABLE OF CONTENTS

LIST OF TABLES

LIST OF FIGURES

Abbreviations and Acronyms

ACRONYM	DESCRIPTION
AHN	Actueel Hoogtebestand Nederland (Dutch National Elevation Model)
BOFDA	Brillouin Optical Frequency Domain Analysis
CH	Cultural Heritage
COMSOL	COMSOL Multiphysics® finite element software
DAS	Distributed Acoustic Sensing
DFOS	Distributed Fiber Optic Sensing
DSS	Distributed Strain Sensing
DTS	Distributed Temperature Sensing
EC	European Commission
FEM	Finite Element Model
FOS	Fiber Optic Sensors
FPH	Flood Proof Holland
GNSS	Global Navigation Satellite System
IA	Innovation Action
KPI	Key Performance Indicator
ML	Machine Learning
NBS	Nature-Based Solutions
RTK	Real-Time Kinematics
SPI	Standardized Precipitation Index
STO	Scientific and Technological Objective
TRL	Technology Readiness Level
TU Delft	Delft University of Technology
WP	Work Package

Executive Summary

Deliverable D9.1 presents the development, calibration, and validation of fiber-optic–based monitoring systems for flood defence infrastructure within the MULTICLIMACT project, with a focus on earthen dikes and movable flood barriers. The work constitutes a key preparatory step toward the real-scale demonstrators and supports the project overarching objective of improving the resilience, preparedness, and responsiveness of the built environment to climate-induced flood and drought hazards. The primary objective of this deliverable was to translate the monitoring concepts defined in earlier project phases into a technically mature and validated solution suitable for deployment in real operational contexts. To this end, Distributed Fiber Optic Sensing (DFOS) technologies were developed and tested to monitor critical physical parameters governing flood defence performance, including temperature, moisture dynamics, pore pressure–related processes, and structural strain. The deliverable addresses both permanent flood defences (dikes) and temporary systems (movable box barriers), ensuring broad applicability across different asset types.

For the dike monitoring system, the work focused on the recovery, tracing, and high-precision mapping of an existing buried fiber-optic cable at the Tedingerbroek dike (Netherlands). Distributed Acoustic Sensing (DAS) and Global Navigation Satellite System (GNSS) surveying were used to reconstruct the cable layout, enabling the implementation of a robust double-ended Distributed Temperature Sensing (DTS) configuration. Field soil investigations and laboratory analyses were conducted to update the hydro-thermal properties of the dike materials, which were subsequently integrated into an updated Finite-Element Model (FEM) hydro-geotechnical model. Extended climatic boundary conditions were applied to quantify moisture, temperature, and pore-pressure dynamics and to derive minimum requirements for sensing frequency, spatial resolution, and temperature accuracy needed to detect relevant changes in stability conditions. For movable flood barriers, a distributed strain monitoring system based on Brillouin Optical Frequency Domain Analysis (BOFDA) was developed. The physical principles governing strain transfer were formalized, and the monitoring architecture—including fiber selection, calibration procedures, and mechanical attachment—was iteratively optimized. Controlled laboratory experiments and living-lab tests at Flood Proof Holland were carried out to validate the strain response, assess robustness under hydraulic loading, and finalize a clamp design suitable for rapid installation and reliable strain transfer during emergency deployment.

Across both applications, fiber-optic measurements were systematically validated against conventional monitoring instruments, including standpipes, moisture sensors, inclinometers, water-level meters, thermal cameras, and strain gauges. This comparative analysis demonstrated that the fiber-optic systems are capable of capturing spatially distributed temperature, moisture, and strain variations with sufficient accuracy and resolution to detect key precursors of failure. While differences between point measurements and modelled responses were observed, these were consistent with expected scale effects and highlighted the added value of distributed sensing for interpreting internal processes that are difficult to observe with discrete sensors alone.

The results show that the developed monitoring systems meet the technical requirements for early detection of abnormal conditions in both dikes and movable flood barriers and have reached a level of maturity suitable for deployment in real demonstrator sites. In addition, the experimental datasets generated in D9.1 provide a solid basis for further model calibration, refinement of installation and operational protocols, and integration with digital early-warning and decision-support tools in subsequent work packages. Overall, Deliverable D9.1 delivers a robust and validated technical foundation for fiber-optic–based monitoring within MULTICLIMACT, directly supporting the upcoming territorial-scale demonstrations and contributing to data-driven, risk-informed management of flood defence infrastructure under changing climatic conditions.

1. INTRODUCTION

This deliverable (D9.1) presents the development and validation of fiber optic–based monitoring systems carried out under Task 9.1 of the MULTICLIMACT project, which addresses materials and technologies for improving resilience at territorial level and their application to a real demonstration case. The work responds to the increasing need for advanced monitoring solutions for flood defence infrastructure under changing climatic conditions, with a focus on earthen dikes and movable flood barriers in the Dutch context. Building on the monitoring concepts defined in Task 3.1, this task aims to further develop, test, and validate the system before its deployment in the demonstrator phase.

The primary objective of the work reported in this deliverable is to validate the fiber optic–based monitoring system under controlled conditions and to quantify its accuracy, robustness, and suitability for operational use. To this end, the system was tested against conventional monitoring instruments, including standpipes, inclinometers, water level meters, and thermal cameras, allowing direct comparison and benchmarking. The experiments were designed to predict and monitor the spatial distribution of temperature, moisture content, internal pore pressure, and deformation in a laboratory dike subjected to controlled environmental loading such as rainfall and water level variations. For the movable flood barrier case, controlled experiments focused on monitoring deformation and leakage through spatially distributed measurements of temperature and strain under hydraulic loading. All experimental activities were conducted at the Flood Proof Holland living lab at TU Delft, providing a controlled yet realistic environment for system development and validation. The acquired sensor data were systematically compared with the response of finite element models developed in Task 4.4, ensuring consistency between observed behaviour and physics-based simulations. This combined experimental–numerical approach enabled refinement of sensing specifications, improved interpretation of distributed measurements, and informed the development of installation and deployment protocols for the demonstrator site foreseen in WP11.

The work was led by Delft University of Technology (TU Delft), which was responsible for experimental design, numerical modelling, system integration, and overall coordination. Fibristerre contributed as manufacturer of the fiber optic interrogators, providing sensing hardware and expertise in distributed temperature and strain interrogation technologies, calibration, and system optimization. RINA Consulting supported the experimental validation, methodological alignment, and integration within the broader project framework. Waterschap Delfland and Waterschap Limburg contributed as end-user partners, ensuring alignment with real-world flood defence management practices, while a Dutch flood prevention company participated as a stakeholder and owner of the movable flood barrier system, providing practical input on operational requirements and deployment constraints.

The results demonstrate that the fiber optic–based monitoring systems are capable of reliably capturing spatially distributed temperature and strain variations relevant to key failure mechanisms in both dikes and movable flood barriers. Validation against conventional sensors confirms the accuracy and added value of distributed sensing under controlled conditions. The outcomes of this work provide a solid technical foundation for improving system accuracy, finalizing installation and deployment protocols, and advancing toward full-scale implementation in the MULTICLIMACT demonstrator. Overall, Deliverable D9.1 contributes directly to the project's objective of enabling continuous, data-driven monitoring to enhance the resilience and risk-informed management of flood defence infrastructure. Chapters 1,2 and 3 describe the general purpose, objectives and overall approach to the system final design and testing. Chapter 4 describes the final fine tunned design of the Dike monitoring system based on new collected information and lab testing. Chapter 5 also included the final design and controlled testing but for the movable barrier system. Chapter 6 describes the movable barrier TRL5 tests at flood proof holland under environmental controlled conditions. Chapter 7 describes the comparison and performance of additional sensors during the tests for better understanding and detection of the system. Chapter 8 is the final designs for the Demonstrator and Finally chapter 9 describes the final design of both systems so that they can be used during the Demonstration.

1.1. PURPOSE AND TARGET GROUP

New shocks and stresses (e.g. droughts) out of the design conditions of the system require innovative solutions to enhance the durability and adaptability of the built environment. The challenge then is to develop better monitoring systems for flood defences capable of detecting abnormalities during heat waves or flood events. This challenged is amplified by the fact that flood defence systems are often very extensive and consequently very heterogeneous in their response to natural hazards which makes them as strong as their weakest element.

The primary objective of this task is to validate and refine the fiber optic-based monitoring system designed in Task 3.1 through a series of controlled experiments at the Flood Proof Holland (FPH) living lab at TU Delft. These experiments aim to assess the system's performance in detecting key failure mechanisms of flood defences and movable barriers—such as temperature variation, moisture content, pore pressure, deformation, and leakage—under simulated environmental conditions including water loading and rainfall. By comparing the fiber optic sensor data with measurements from conventional sensors (e.g., standpipes, thermal cameras, inclinometers), the experiments will evaluate the system's accuracy and reliability. The outcomes will inform the development of installation and deployment protocols for the Dutch demonstrator site and support the calibration of FEM models developed in Task 4.4, ultimately contributing to the enhancement of flood resilience strategies within the MULTICLIMACT project.

1.2. CONTRIBUTIONS OF PARTNERS

*The following table (*Table 1. Contributions of Partners*) shows the main contributions from project partners in the development of this deliverable.*

PARTNER SHORT NAME	CONTRIBUTIONS
TUDELFT	Definition of the final demo site layout, development and calibration of the monitoring system, FEM models validation. Report writing of Chapters 4, 6, 8, 9, 10 and sections 5.3,5.4
FIBRISTERRE	Setting the parameters of the hardware for the acquisition and design further enhancement. Report writing of Chapter 7 and sections 5.1, 5.2 and 5.4.
RINA-C	Support in experimental campaign. Report writing of Chapters 1, 2, 3.
DELFLAN and WL	Support during the testing and Demonstrator logistics with several meetings.

Table 1. Contributions of Partners

2. OBJECTIVES AND EXPECTED IMPACT

2.1. OBJECTIVES

Within the framework of Task 9.1, the primary objective was to **experimentally demonstrate and validate the performance of a fiber-optic-based monitoring systems under controlled laboratory conditions for both dike and movable barriers**, as a preparatory step for its application in the Dutch demonstrators. Deliverable D9.1 documents the different numerical and physical models and tests performed as a series of laboratory experiments conducted at the Flood Proof Holland living lab and TU Delft Mechanical and Structures lab, where representative dike and movable barrier elements were instrumented and monitored under well-defined environmental loading scenarios. In addition, FEM models of the dike and clamps are also presented as they helped to fine tune the system in prior preparation for the demonstrators. A key objective addressed in this deliverable was the **implementation of distributed fiber-optic sensing technologies in realistic flood protection structures (box barriers and dikes)** and the assessment of their capability to monitor relevant physical parameters. In the later stage, these parameters are going to used as input for evaluating the different defence's structural performance. In D9.1, fiber-optic cables were installed and tested within and along the actual Tedingerbroek dike, and Dike lab (Flood Proof Holland) for the box barrier components, enabling continuous measurements of temperature and strain along the different monitored sections and sensor clamping systems. These installations allowed the response of the structures to controlled water loading and rainfall conditions and mechanical tensile loading to later be observed and analysed with high spatial resolution, demonstrating the feasibility of the proposed sensing technologies in complex extreme weather, mechanical and geotechnical conditions.

Another central objective of Task 9.1, as implemented in D9.1, was the **experimental validation of the** sensor's data based on in-point analogous sensors. This objective is also reflected in this deliverable by presenting and discussing measurements obtained from standpipes, thermal cameras, inclinometers, and water level sensors, which were used as reference data sets and later compared with the collected signals from the fiber optics-based sensors. By comparing the temporal and spatial evolution of these signals obtained with respect to the different sensing systems, the deliverable provides an assessment of the accuracy, sensitivity, and reliability of the fiber-optic monitoring system, while also illustrating its advantages and disadvantages in terms of having spatially distributed coverage and higher frequency.

Moreover, the objective of **characterizing spatial distributions of temperature, deformation, and hydraulically induced processes** within the monitored structures is also discussed in detail. These experimental results are reported in D9.1 to demonstrate how distributed fiber-optic measurements can be used to identify zones affected by water infiltration, thermal gradients, and mechanical strain (displacements and deformations) response, supporting the interpretation of internal processes that are difficult to capture using discrete sensors alone. For the movable barrier experiments, the monitoring approach was applied to detect deformation and potential leakage paths, with independent confirmation provided by thermal imaging and water level observations.

Finally, the objective of **supporting modelling activities and future field deployment** by providing experimental data suitable for comparison with finite element model responses developed in Task 4.4 is also included. While the focus of the deliverable is on experimental validation, the documented measurements establish a basis for model comparison and calibration and have been used to identify practical aspects related to sensor installation, data interpretation, and system limitations. These outcomes directly inform the preparation of deployment and operational protocols for the Dutch demonstrator in WP11.

2.2. EXPECTED IMPACT

The expected impact spans technical, operational, and socio-economic dimensions:

- **Early detection & risk reduction:** Distributed sensing increases observability of failure precursors—thermal anomalies linked to seepage, rapidly evolving moisture fronts, localized strain peaks—supporting timely interventions that prevent breaches, reduce emergency response costs, and enhance public safety.
- **Preparedness & response:** Higher measurement frequency and spatial granularity improve nowcasting of asset condition during extreme events (storms, prolonged rainfall, heat waves). This directly strengthens resilience pillars—preparedness (anticipate), absorption (withstand), and rapid recovery (restore).
- **Optimized maintenance & lifecycle:** Continuous condition data enables risk-based inspection, prioritization of remediation works, and smarter strengthening programs. Over time, this reduces OPEX and defers CAPEX by targeting interventions where they deliver the greatest benefit.
- **Interoperability & scalability:** Architectures based on widely adopted IEEE/ITU/IEC sensing technologies and modular interrogators foster interoperability with existing telemetry and digital twins. Linear assets (dikes, canals, pipelines, rail embankments) benefit from similar sensing logic, making solutions scalable across territories.
- **Evidence-based policy & public value:** Better data improves risk models, fragility curves, and resilience KPIs, supporting transparent, evidence-based policy choices and market innovation around resilient infrastructure services.

3. OVERALL APPROACH

To achieve the objectives defined in Task 9.1, on the **progressive development and experimental validation of a fiber-optic-based monitoring system under controlled laboratory conditions**, as a prerequisite for its future application in the Dutch demonstrator. In line with the description of Task 9.1, the work focused on translating the monitoring system designed in Task 3.1 into a validated solution through systematic testing in a realistic but fully controlled environment.

The first step of the approach consisted of **defining the experimental scenarios and monitoring objectives** relevant to flood protection infrastructure. Based on the target application at territorial level, the experiments were designed to investigate the system's ability to monitor key physical quantities associated with dike and movable barrier performance, including temperature, deformation, moisture-related processes, and hydraulically induced responses. Controlled environmental conditions, such as water loading and rainfall, were selected to ensure repeatability and to isolate the response of the monitored structures.

The second step involved the **deployment and integration of the fiber-optic monitoring system within the Flood Proof Holland (FPH) living lab at TU Delft**. Distributed fiber-optic sensors were installed in laboratory dikes and along movable barrier elements, following layouts representative of realistic monitoring configurations. At the same time, existing conventional instrumentation at the facility—such as standpipes, inclinometers, thermal cameras, and water level sensors—was incorporated into the experimental setup to serve as reference measurements for validation purposes.

The third step consisted of **executing controlled experiments on laboratory dikes**, during which the fiber-optic system continuously acquired spatially distributed measurements under imposed hydraulic and environmental loading conditions. These experiments aimed at predicting and analyzing the spatial distribution of temperature, deformation, and internal processes related to moisture content and pore pressure. The fiber-optic measurements were systematically compared with data from the pre-installed sensors, enabling an assessment of measurement consistency and sensor accuracy under controlled conditions.

In parallel, a dedicated set of experiments was conducted for the **movable barrier case**, focusing on the monitoring of deformation and leakage phenomena. Distributed temperature and strain measurements obtained from the fiber-optic system were used to identify potential leakage paths and structural responses. These observations were validated using additional sensors installed along the barriers, including water level meters and thermal cameras, providing independent confirmation of the detected phenomena.

Finally, the collected experimental data were **analyzed and interpreted in relation to numerical model expectations**, by comparing the measured responses with the FEM model results developed in Task 4.4 for the laboratory dike configurations. This comparison supported the evaluation of the monitoring system's capability to capture relevant structural behaviour and provided feedback for improving measurement accuracy. The overall experimental process documented in Deliverable D9.1 generated practical knowledge on sensor performance, installation, and data interpretation, forming a validated basis for the development of installation and deployment protocols to be applied in subsequent demonstrator activities.

4. FIBER OPTICS BASED DIKE MONITORING SYSTEM FINAL CONFIGURATION AND INSTALATION

The dike monitoring system is based on distributed fiber-optic sensing technologies designed to provide continuous, spatially resolved monitoring of key physical processes governing dike performance, including temperature variations, moisture dynamics, and related hydro-geotechnical behaviour. The system relies on a buried fiber-optic cable installed within the dike body (see Figure 1 right image), connected to an on-site interrogator that performs distributed temperature measurements and, where required, acoustic or strain-based sensing. The system is validated based on in-situ sensors such as multi-depth moisture sensors (see Figure 1 left image),

Figure 1 Left image: GSM moisture content sensor installed in the same location of the embedded fiber optic cable. Right Image: Lateral view of the Tedingerbroekpolder dike.

To operate reliably, the system requires accurate knowledge of the cable layout, stable power supply, protected housing for the interrogator, and a data acquisition and communication setup enabling continuous recording and storage of measurements. In addition, appropriate calibration procedures, reference measurements, and supporting numerical models are needed to interpret the sensor data in terms of moisture evolution and stability conditions, ensuring that the monitoring system delivers actionable information for early warning and asset management.

4.1. UPDATED CABLE LOCATION

To give context and a background to this activity, the Tedingerbroek Dike was reinforced with a clay layer of 50 cm in the year 2015 by Delfland, which is the managing authority of this dike. At that time, a fiber optic cable was laid and buried with the clay layer, at an average depth of 40 cm. However, during installation, precise coordinates of the cable were not recorded, and they only relied on human memory in locating the place where the cable was installed. Now with the MULTICLIMACT activities coming in about 10 years later, where changes of staff within the waterboard happened and they could no longer tell where the cable was installed, it was almost impossible to find the location of the end point of the cable and the cable itself.

4.1.1. CABLE TRACING

The project team had to come up with creative means of tracing the location of the cable and the end point of the fiber cable. This end-point was very critical to achieve double-ended measurements

during the monitoring campaign. To do this, there was a need to splice the end point of the cable, single-mode to single-mode fiber and multi-mode to multi-mode fiber.

Since the installed cable had a metal jacket, the project team first went to the field with a metal detector (Figure 2) which had the ability to detect any metal present in the soil within an average depth of 40 cm. However, this method proved to be not good as there are a lot of impurities in the dike, leading to continuous beeping which were false positives with regards to the location of the cable. In addition to that, this dike has a sheet pile and a continuous longitudinal metal fence to protect sheep from falling into the water, so every time the metal detector was taken closer to the fence, it would beep. Within the dike there was also several foreign metal objects such as stand water level pipes, sheet piles and other equipment that generated interference and made the cable location very uncertain.

The second option in tracing the cable was to use DAS technology was utilized (Figure 2 right image). This technique is based on Rayleigh scattering which exploits the proportionality between the interferometric light phase change and the change in the vibration signal measured by the interferometric acoustic sensor. It is also an interrogation unit that gets connected to the same existent cable but is capable of recording strain variation in a broadband of frequencies at any location along the cable. With DAS, vibrations and acoustic events can be recorded and spatially resolved over tens of kilometres. A constant weight of 8 kilograms was dropped several times from a fix height of 1 m at intervals of 5 m distance along the suggested cable length and the differences in magnitude of the amplitudes were observed, which precisely told the location of the cable in the ground.

Figure 2 Nokta Simplex metal detector for cable tracing

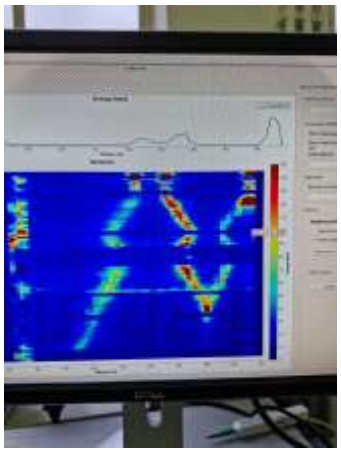

Figure 3 Shows the DAS signal strength when the weight of 8 kgs was dropped from a height of 1 m.

4.1.2. CABLE MAPPING

To Map the exact location of the cable in the dike, we used Leica GPS. Its receivers have robust signal availability even in challenging environments because its receivers use multiple constellations. This was preferred due to various reasons; it was already existent within the university faculty, its high-level precision with Real-Time Kinematics corrections (RTK) also made it perfect for mapping as the cable location precision was critical.

The Leica GPS is also fast and efficient because it rapidly acquires satellite signals and fix positions immediately. It was also very easy to collect data from the GPS as we could easily send the data

through email whilst still in the field, as compared to other traditional surveying methods that take significant time. It was also advantageous to us because the GPS was fast as you did not need to mount the tripod, the base and connect the rover as compared to the traditional differential GPS, significantly reducing the amount of time spent in the field.

With the help of Delfland, the project team was able to come up with an initial path of the cable which provided an idea of where to start from in tracing of the cable. The image below shows the sketched map, which got the shape of the layout correct, but was shorter with approximately 100 m. After tracing the cable with the DAS, the precise location of the cable was determined, which was found to go further than what was initially sketched based on historical information. After processing the data from the GPS, the following map of the cable was prepared. To present a better understanding of the initial and actual location of the cable, the actual location (represented by the green line) was overlaid on top of the suggested location (in yellow).

Figure 4 Shows the initially assumed positioning of the cable, based on historical data

Figure 5 Exact location of the cable (in green) which was overlaid with the initial thought of the cable position.

The endpoint of the cable (located at the end of the green line in the most left side of *Figure 5*) was then exposed and properly encased with protection in a polycarbonate plastic enclosure and put back in the ground at a depth of 40 cm below ground levee, as can be seen in the picture below. This end point location is not only important to have the correct mapping in space but also for calibrating the cable under controlled thermal conditions.

Figure 6 Left image: location of the end-point of the cable, which has a coil of cable of approximately 10 m. Right image: Interrogator location inside the pumping station.

4.1.3. DATA COLLECTION

The positioning of the interrogator was located at one end of the line close to the pump house (see *Figure 6*), directly above the cable route and started recording the points every 5-10 m. Discrete points along the cable where recorded as opposed to continuous logging because there were significant changes in direction and elevation between the crest, the slope, and the toe. To maintain precision and quality of the collected data, all data points were fixed. In some cases, we would re-measure critical points, for example, the location of the end point of the cable and in areas where we had bends, critically checking the spacing and completeness at every data point. The data collected was then exported directly from the equipment through email. It can send data in CSV, DXF, SHP, KML, or GIS database, with the option of including attribute tables if required. In this project, the data was exported in KML format, which is also acceptable in QGIS for generating maps and used in COMSOL Multiphysics software for post-processing, using it as an input for modelling.

4.1.4. DOUBLE ENDED MEASUREMENTS

With DTS technology, one can choose to either run single ended measurements or double ended measurements. In single ended measurements, only one end of the fiber optic cable is connected to the interrogator. The system then sends a laser pulse and measures the backscattered light that returns from various points along the fiber. However, there is a lot of signal attenuation, and the system accuracy reduces over long distances of measurement. To overcome this, double-ended measurements are preferred, where the optical fiber is looped back so that both ends of the fiber are connected to the interrogator which allows the system to send and receive signals from both directions through the same fiber. The image below shows the details of the spliced cables. To overcome problems of accuracy, the team resorted to using double ended measurements to cancel out signal attenuation. The cable in the dike has four fibers inside, two single mode and two multi-mode. Using the Fujikura 62 + cable splicer, which solders broken fibers together by fusion technology, the ends of each of the two analogous cables where spliced; the single mode to single mode cable and multi-mode to multi-mode cable so that two times the length can be interrogated on one single laser shot. This is called Double-ended measurements and serve as an advantage in identifying exact location of faults or when the cable breaks, by comparing the signals in both directions.

4.1.5. CABLE SPLICING

After locating the end point of the cable with the DAS, there was a need to splice the cable so as to achieve double ended measurements to improve the accuracy and reliability of the measurements. For single ended measurements suffer (Danka and Zhang 2015) from attenuation especially over long distances of measurement, where the strength of a signal is lost along the fiber which may distort temperature readings.

Figure 7 Lef image: Shows the spliced fiber cables in a polycarbonate plastic box. Center image: Splicer during soldering procedure. Right Image: Control Room installation.

With the above cable setup, the project team is now able to run continues monitoring campaign by taking temperature measurements every 30 minutes.

4.1.6. CONTROL ROOM

A pump housing facility is located at the northern part of the dike, with constant power supply, belonging to our partner Delfland where they manage the daily operations of the pump. With their arrangement and permission, they provided one of the rooms to TU Delft to setup the equipment (see Figure 7) to shield it from direct sunlight, dust and rain which could damage the electrical components of the system. The cable is connected to an interrogator unit that is housed on site, in the pump house for Delfland.

4.2. SYSTEM UPDATED MINIMUM SPECIFICATIONS

As explained in the previous chapter, the original location from the cable was re-evaluated with more accurate technology given the discrepancy between measurements and reported original location. Hence, a new FEM model was built to correct for the topography difference and the location of the cable while using a new soil parameterization site investigation of the upper layer which is the most important for the rain infiltration process.

4.2.1. SOIL INVESTIGATION

To determine the soil composition of the dike, there was a need to collect soil samples from the dike and conduct detailed tests in a lab. A total of six samples were collected from 6 random points within the dike. Probes were used to collect 60 cm depth of sample. Since this exercise was done in summer when the dike was too dry, it was a bit difficult to drill through the first few centimetres of the clay dike as it was too dry. Below are the pictures during the process of sample collection.

Figure 8 Shows the probes being extracted from the ground for sample collection at different locations.

4.2.2. LAB ANALYSIS OF SOIL TEXTURE FROM SAMPLES

The texture of soil describes the relative proportions of soils with representative diameters of the three main fine grained texture groups (sand, silt and clay) which is a stable and almost permanent physical characteristics as it requires geological time spans to change significantly. It is used in the lab as a classification tool from which different pedontransfer characteristics and functions can be inferred using large world broad data bases such as the Rosetta (Borek et al. 2021).

In the Geosciences lab, a hydrometer test was performed in six different soil samples of the same layer over the dike. This is a widely used method for determining the distribution of particle sizes in fine textured dominated soils for which the silt range (63-2 μm), and the percentage of clay minerals < 2μm is higher than 30% between the two textures. Note that, the test is usually not performed if less than 10% of the material passes the 63 μm sieve (silts) which will show a coarse textured material dominating the sample. The hydrometer analysis utilizes the relationship among the velocity of fall of spheres in a fluid (Stoke's law), the diameter of the sphere, the specific weights of the sphere and of the fluid, and of the viscosity of the fluid. Note that anthropogenic manipulated soils located in the surface of such structures also contain a large portion of organic matter due to either decomposition of vegetation or the active one such as grass, roots and biological activity e.g. insects or bacteria colonies.

Figure 9 Shows a freshly collected sample, ready to be weighed before being dried in the oven

Figure 10 Shows the six soil simples ready to be weighed after they were dried in the oven at 105 Degrees Celcius for 24 hours

Later on, the samples are dried so that the organic matter is decayed and water content is evaporated by placing the cores inside the oven at a temperature of 105^0C for a period of 24 hours. From the oven, the weight of the dry samples was measured and recorded so that the total inorganic part weight is stablished before placing the soil samples in the hydrometer. To determine the granulometric compositions (particle size distribution), a standard sieving method is applied for which the soil sample is placed and vibrated over a set of nets that follow ASTM C136 standard for soil (Boschert and Howard 2015) as shown in Figure 11.

Figure 11 Left Image: ASTM C136 standard sieve test Right Image: Finer Particle Settlement Procedure

Based on the 6 samples, an average granulometric curve (Figure 11) was then produced where a final texture classification while discarding organic matter. This distribution allows to use the Unified Soil Classification System (USCS) AASHTO to determine the type of soil based on its component textures. From the sieve curve, 55% is sand, 22% is silt and 23% is clay corresponding to a **Sandy-clay-loam** (on the sandy side) type of soil as shown by the red dot (FIgure 12 right image).

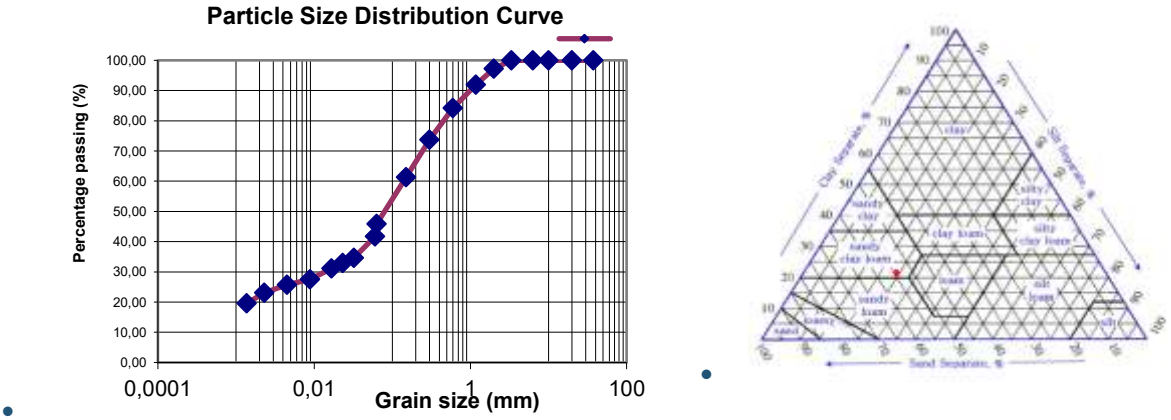

FIgure 12 Left image: Average sieve granulometric curve. Right Image: Upper dike layer Soil classification based on texture.

The soil main characteristics regarding the material physical description is presented in Table 2 where all values for describing the type of soil based on international standards and coefficients derived from linear interpolation inside the sieve curve.

CHARACTERISTIC	VALUE	NOTES
Sand Fraction (0.05-2.0 mm)	55.25%	Normalized for USDA texture triangle (original: 53.72%)
Silt Fraction (0.002-0.05 mm)	22.16%	Normalized for USDA texture triangle (original: 21.55%)
Clay Fraction (<0.002 mm)	22.58%	Normalized for USDA texture triangle (original: 21.95%)
USDA Texture Classification	Sandy Clay Loam	Based on sand (55%), silt (22%), clay (23%) in USDA triangle
Gravel Fraction (>2.0 mm)	2.78%	100% - 97.22% (passes 2.0 mm)
Fines Fraction (<0.075 mm)	~48%	Interpolated between 0.063 mm (45.87%) and 0.150 mm (61.29%)
D60 (Grain size at 60% passing)	0.161 mm	Interpolated between 0.150 mm (61.29%) and 0.300 mm (73.73%)
D30 (Grain size at 30% passing)	0.0137 mm	Interpolated between 0.00889 mm (27.54%) and 0.01669 mm (31.10%)
D10 (Grain size at 10% passing)	<0.00137 mm	Below smallest measured size (0.00137 mm at 19.55%), not precisely known
Uniformity Coefficient (Cu)	Not calculable	Requires D10, which is below measured range
Coefficient of Curvature (Cc)	Not calculable	Requires D10, which is below measured range
USCS Classification	SC (Clayey Sand) or SM (Silty Sand)	SC if fines are plastic; SM if non-plastic; based on ~48% fines, no gravel

Table 2. Dike cover properties from sieve curve results.

In the previous Phase of the MULTICLIMACT project, average values from literature for a sandy clay were used as reference for the finite element model. Now with the actual data, the information has been updated for the upper layer for a sandy clay loam. Based on the texture results, the Rosetta database (Schaap et al. 2001) is used to infer the new water retention parameters which will describe the soil matric potential relation with respect to the moisture content of the soil and its infiltration capacity and hydraulic conductivity. In the previous Phase of the MULTICLIMACT project, values from literature for a sandy clay loam were used as reference for the finite element model. Now with the actual data the information has been updated for the upper layer as:

PARAMETER	VARIABLE	UNIT	SANDY-CLAY-LOAM (UPDATED)	CLAY (LITERATURE)	PEAT (LITERATURE)	SAND (LITERATURE
Saturated hydraulic conductivity	K_s	[m/s]	9.25e-6	~~1e-5~~	6e-4	5e-3
Air inflow parameter	α	[1/m]	10.9	~~8.3~~	8	3.4
Texture exponent	n	[-]	1.8	~~1.4~~	1.75	1.15
Saturated water content	θ_s	[m3/m3]	0.4169	~~0.565~~	0.93	0.45
Residual water content	θ_r	[m3/m3]	0.0795	~~0.137~~	0.32	0.135

Table 3 *Updated Hydrogeologic material parameterization for new FEM*

Note that the other reference values are not necessary to be updated as the water levels of the channel a groundwater system have too little variation which implies that most of the fluxes occur in the saturated zone where the pean and sand layers are completely submerged. Hence, it is expected that most of the moisture variation of the vadose zone will be in the clay upper layer and mostly driven by rainfall and drought. The thermal parameters are kept unmodified with respect to the previous MULTILCIMACT project phase as these are withdrawn from literature. Hence the same table presented in D3.1 is repeated here for reproducibility.

Table 4 Geothermal material parameterization from D3.1

PARAMETER	VARIABLE	UNIT	CLAY	PEAT	SAND
Thermal conductivity	$-\lambda_{eff}$	[W/(m*K)]	2.9	0.25	8.4
Fluid Density [Water]	ρ	[kg/m^3]	1000	1000	1000
Heat Capacity	C_p	[J/(kg*K)]	800	1920	730
Dry bulk density of soil	ρ_s	[Kg/m3]	2650	1350	2600

4.3. NUMERICAL MODEL: UPDATED FEM MODEL

Based on the findings and update of the new cable location (green line in Figure 13), a new FEM model has been built with respect to the one reported in the first phase of the MULTICLIMCAT project in deliverable 3.1. This new updated finite element model has been changed in terms of its topography, soils parameterization and boundary conditions time series. Note that while the expected infiltration response could be similar, the layering in the model changes with space so in the new model, the soil layers are thicker which may result in different fluxes in the saturated zone. Also, the spacing between points along the cable became more certain with the new mapping and they reflect a wider distance between cable lines.

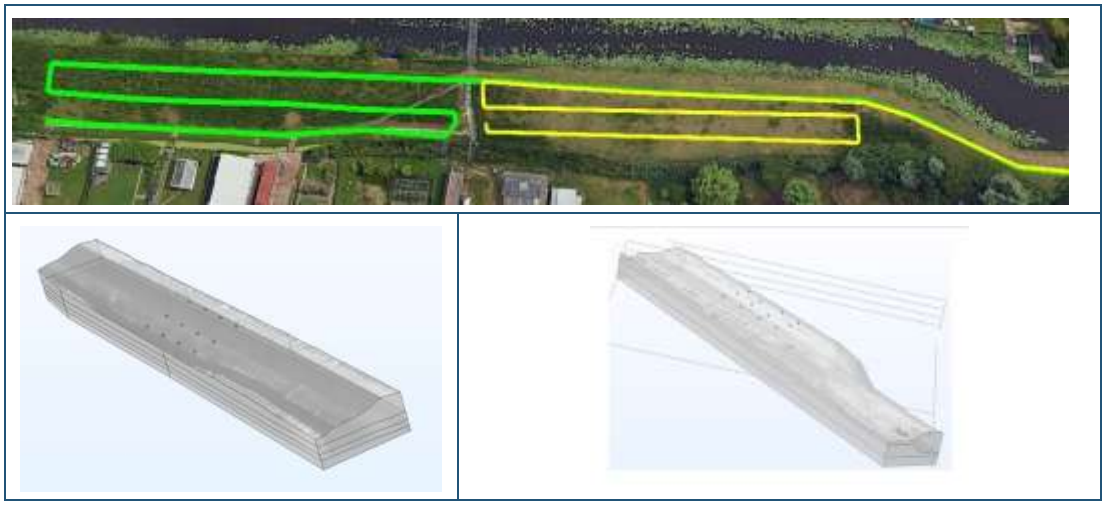

Figure 13 Updated topographic Interpolated Surfaces and generated Mesh from 3D finite element model produced in COMSOL Multiphysics (204,029 Tetrahedral Elements) with AHN4 surface input. Left side: Updated cable location and corresponding finite element domain. Right side: Original Finite element model 3D domain used in the first phase of MULTICLIMACT.

4.3.1. UPDATED BOUNDARY CONDITIONS

An important finding for the present demonstrator is that the side channel which discharge the flow from inland towards the coast by the downstream present pump is not influence in inner phreatic level inside the dike. After talks with the operators of the pump and installing two different pressure divers along the interface between the dike and channel, it was found that the channel is lined with a geotextile that prevents the inflow from the channel toward the dike. This is a very good finding as it means that the dike inner moisture is mostly driven by rainfall giving a broader range of hydrological cycles for the fiber optics cable to detect.

At the start of the MULTICLIMACT Project, preliminary models based on expert knowledge and shorter time series (350 days – year 2023) as the monitoring of water levels and rainfall time series were used to the availability possible with respect to the milestones of the project in the first phase (Plan and design). For the present deliverable, a longer time series of 912 days (2.5 years starting 01-01-2023 until 15-06-2025) where used for all required time series that include available for water levels, rainfall time series and environmental temperature which represent the main inputs of the FEM model. This allowed to included even more extreme rainfall events on the simulation which were not included in the previous estimation for rainfall events with intensities above 5 mm/h as it can be observed in Figure 14.

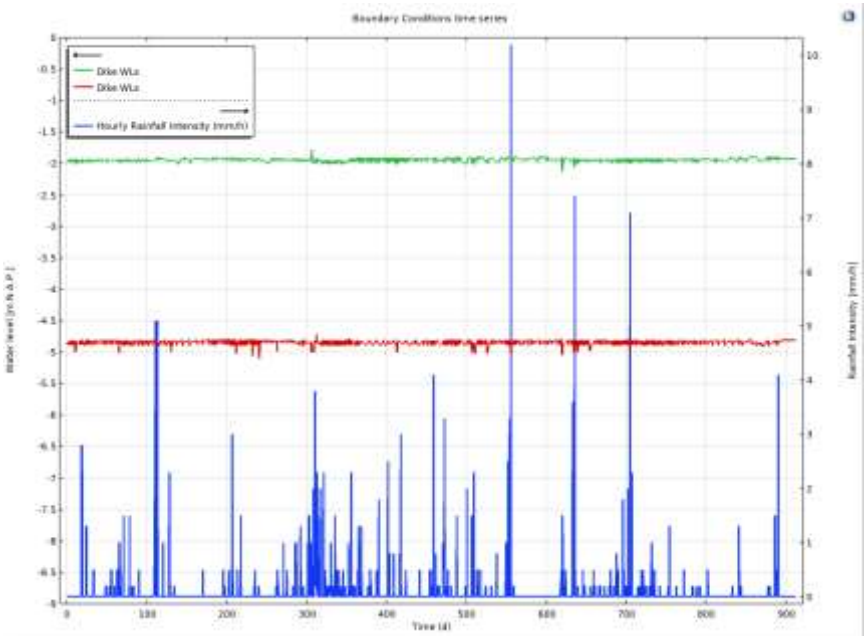

Figure 14 Boundary conditions time series used to simulate the water fluxes inside the dike during the first 912 days (01-01-2023 to 15-06-2025). Green line corresponds to the phreatic table level (Water load) in front of the dike. Red line corresponds to phreatic level on the right side of the dike (Polder phreatic level). Green bar plot correspond to the events of rainfall in intensity units (mm/h) during the whole time span of simulation.

Same principle applies for the thermal boundary conditions for which longer time series where also used in the new simulation 912 days (2.5 years starting 01-01-2023 until 15-06-2025) for capturing the environmental temperature. This also allowed to capture 2.5 full hydrological cycles including the diurnal and nocturnal component of the cycle as shown in Figure 15.

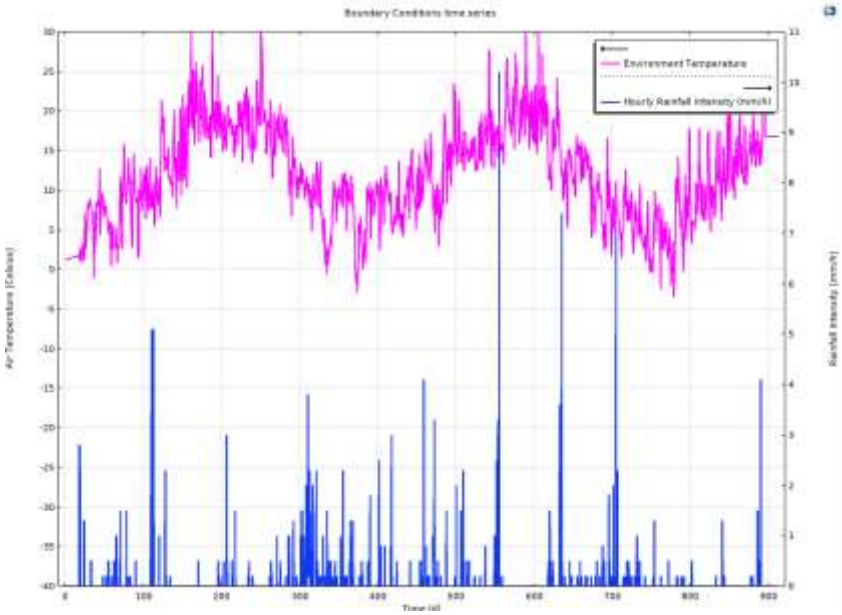

Figure 15 Boundary conditions time series used to simulate the environmental temperature outside the dike during the first 912 days (01-01-2023 to 15-06-2025) and Rainfall events along the same period.

4.3.2. SENSOR REQUIRED FREQUENCY BASED ON MOISTURE CONTENT CHANGE

To determine the minimum frequency, the derivative of the moisture signal with respect to time ($\frac{\partial S_r}{\partial t}$) is estimated from the Richard's equation based FEM updated model along three points located at each of the cables as shown in Figure 16.

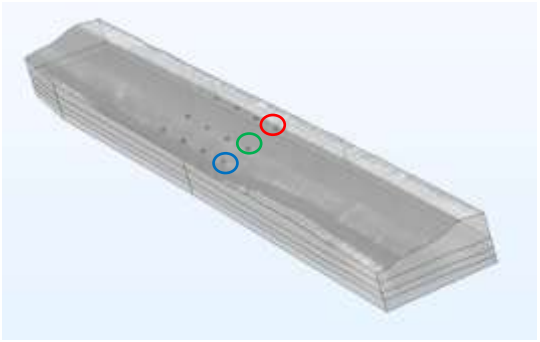

Figure 16 Locations for signal extraction along the three different cable lines in the updated FEM model.

For the raw signal (Figure 17), it can be observed that in the new model and because the new boundary conditions, topography and parameterization the response change significantly showing the largest moisture variations in points located in the toe (blue line). Moreover, the three locations now show to be significantly more responsive since the groundwater level boundary condition makes them drier during the year while remaining with larger storage capacity to store rain events.

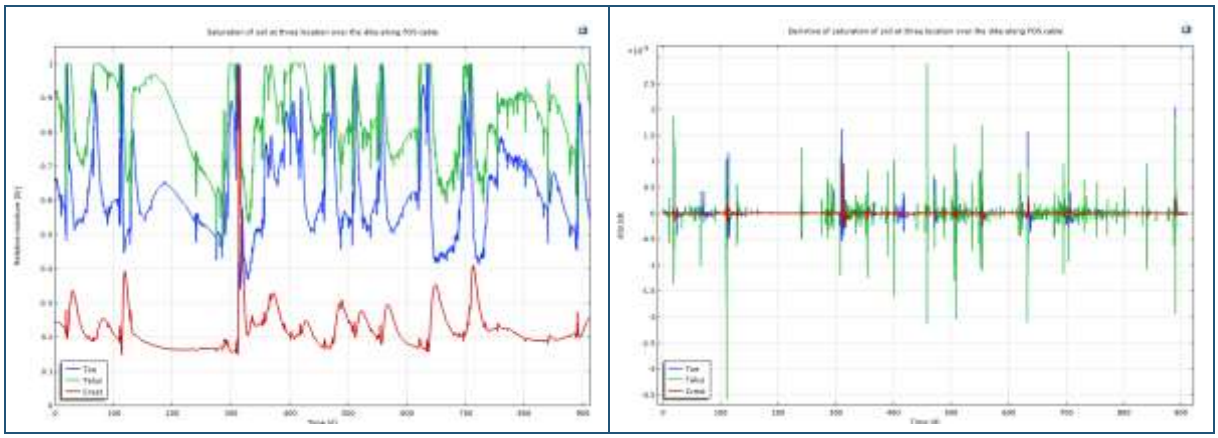

Figure 17 a) Calculated relative moisture content in different cable locations along the year 2023 b) Rate of change of moisture with respect to time.

This will represent in hindsight a larger reduction of effective stresses in the soil due to the reduction of matric suction and consequently larger stability safety variations. It also shows an extreme rainfall event around the 300 days which results in full saturation of the complete dike. It is expected that days like this, can result in unsafe situations for which measure should be taken. If predicted in advance, the model proves the value of the monitoring system for increasing the resilience of the build environment.

From the derivative of the signal (Figure 17b), it can observe that the fastest rates of moisture changes are obtained for desiccation rate along the talus on day 110 with a -3.58e-5 1/s and 3.11e-5 1/s on day 705 also for the talus location but in terms of saturation rate. This is 2.5 times faster than previously estimated on the former FEM model. With these values in mind and assuming that the system should be capable of determining changes in moisture of 1% as stated in the design phase of MULTICLIMACT, the monitoring system will require a frequency of measurement of 279 seconds for desiccation and 321 seconds for saturation. These new values require an almost 2 times faster recording capacity for the system with respect to what was estimated in the design phase (98 and 286). Now it is also important to note that the variations of the moisture content of 1% will only be captured given the Nyquist-Shannon principle of analog signal monitoring which states that the signal can only be digitized without an aliasing error only if its sampling rate is greater or equal than twice the highest frequency of the desired signal to capture. This means that the system will require to measure the moisture/temperature for both desiccation and saturation frequencies along the fiber close to every 2 minutes 19 seconds and 2 minutes 40 seconds respectively. It's also important to note that 1% moisture change is quite ambitious value and that even if achieved, it is only useful for situations close to full saturation where the effective stresses inside the soil result in situation close to failure. However, the actual specification of the DFOS interrogator which is in charge of withdrawing the distributed measurements of temperature is still capable of interrogating a 10 km cable in less than 2 minutes.

If a similar exercise is performed is done based on the pore pressure change signal in the same three location of the cables, it can be estimated what is the rate of change of pressure. From the raw signal while the largest moisture content change occurred in the talus location, the largest pressure head change occurs in the crest (see Figure 18a). The reason for this is that as it is the location with the highest elevation with respect to the phreatic line, the inner pore pressures are more negative while being closed to the upper boundary condition driven by rainfall. Nonetheless, it is expected that the three different locations will have the same usefulness at the moment of inferring the location of the phreatic line as all of them represent a point in the soil water retention function of the soil.

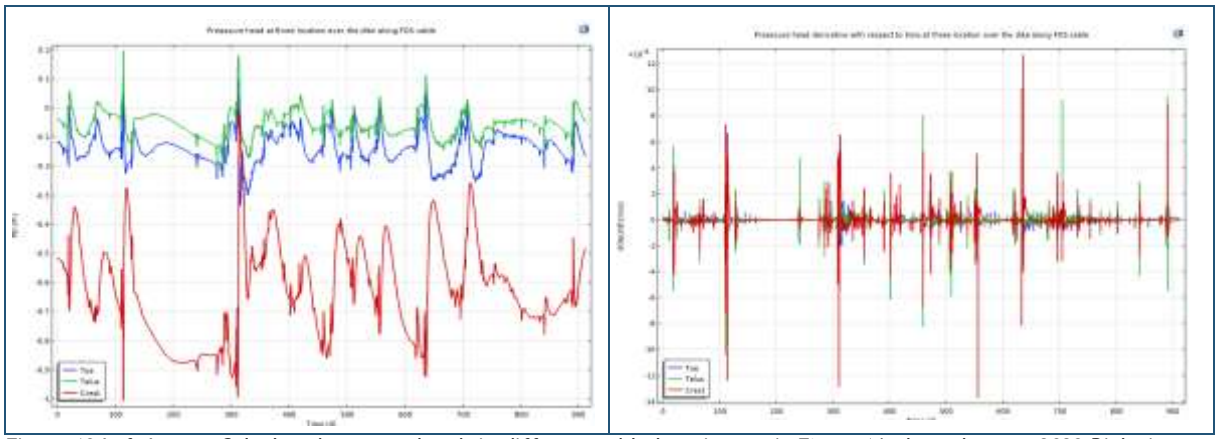

Figure 18 Left Image: Calculated pressure heads in different cable locations as in Figure 16 *along the year 2023 Right image: Rate of change of pressure heads with respect to time in the same locations.*

From the derivative of the signal (Figure 18b), it can be determined that the highest rates of decompression and pressurization in time are observed in the crest location at 556 and 636 with -13.76e-6 and 12.73e-6 m/s. If we use the recording frequency found in the moisture signal derivative (139 seconds/1% Sr), it will mean that we will be able to capture pressure head changes of maximum -0.19 cm and 0.17 cm every 139 seconds (2 minutes and 19 seconds). These are very rapid changes which are expected to occur during extreme events but far from average operational conditions. This means that in case that similar pore pressure changes are expected to be recorded, the frequency of recording requires to be reduced so that enough change can be observed.

4.3.3. SENSOR FREQUENCY REQUIREMENT BASED ON TEMPERATURE CHANGE

A similar analysis as the ones reported in the previous section was performed but in this case by using the temperature signal in the same three locations. Note that this signal is assumed to be equivalent to the one expected to be recorded by the FOS distributed temperature monitoring system which is going to be later used as main input to infer the moisture content. This signal is presented later in the analysis while it is captured before than the inference of moisture and the reason is because in the model, the temperature signal is affected by the environmental temperature and the moisture content which changes the thermal properties of the soil such as thermal capacity and thermal conductivity. The obtained signal in the three different places is plotted along the environment signal (Figure 19 Left) and it can already be observed that the amplitude of the signal in the cable is smaller than the one of the environment as the soil and water composed medium works as a thermal insulator. Nonetheless, while all three locations are exactly below 40 cm for the surface, it can already be observed that the talus point is the one that presents the highest temperature by a small margin with respect to tother points. However, it does have a significant difference during the cooling phases. This is explained by the fact that this point is the one with more water content in average along time which is a better temperature conductor than air. Moist soil conducts temperature better than dry soil as the water particles that filled the porous cavities, increasing the thermal conductivity of the overall granular system allowing it to cool faster.

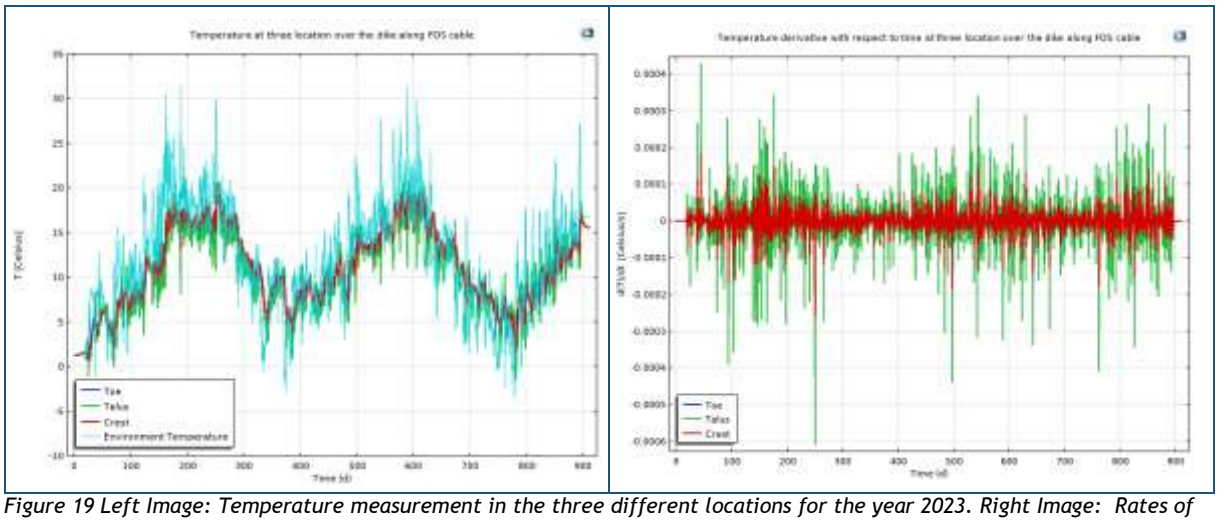

Figure 19 Left Image: Temperature measurement in the three different locations for the year 2023. Right Image: Rates of change of temperature

From the derivative of the signal, it is also observed that the point in the talus presents the fastest heating and cooling rates (Figure 19b) at the start of the simulation on the day 44 With 0.00044 Celsius/sec and 0.0006 Celsius/sec on the day 250. Note that the day 250 is not the coolest of the time series as the thermal process is also characterized by a delay in the signal derived from the moisture change. With these rates in mind, it can be estimated that the system will be capable of detecting an increase of temperature of 0.061 Celsius and 0.083 Celsius decrease if record every 2 minutes 19 seconds which is the minimum recording frequency required by the system. Note that a change of 1 Kelvin is equivalent to the change of 1 Celsius and the Fibristerre DTS interrogator can detect events ±0.001 Kelvin. These results show that the interrogator will be more than capable of detecting the temperature required accuracy for the expected moisture change.

4.3.4. SENSOR MINIMAL SPATIAL RESOLUTION BASED ON MOISTURE CONTENT

The moisture content distribution is modelled inside a 3D volume for which the FEM software builds the numerical solution for the given mesh. This volume was built following the digital elevation map AHN4 of the Netherlands with a resolution of 5 [cm] pixels. This means that the most relevant topographic variation along the cover is captured in our updated model and therefore while using constant hydrogeological parameters per layer, there is still some variation in the infiltration patterns due to the surface irregularities as shown in Figure 20:

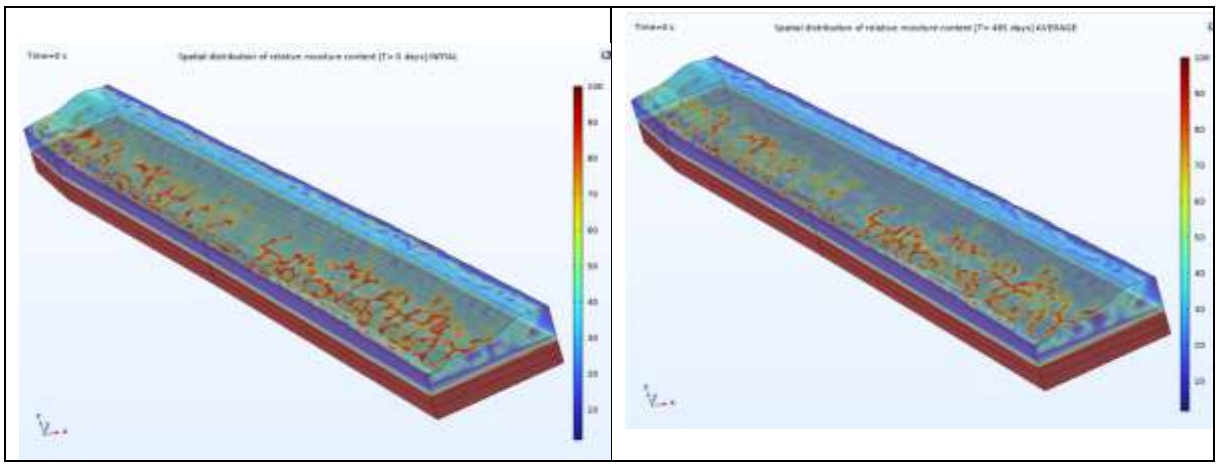

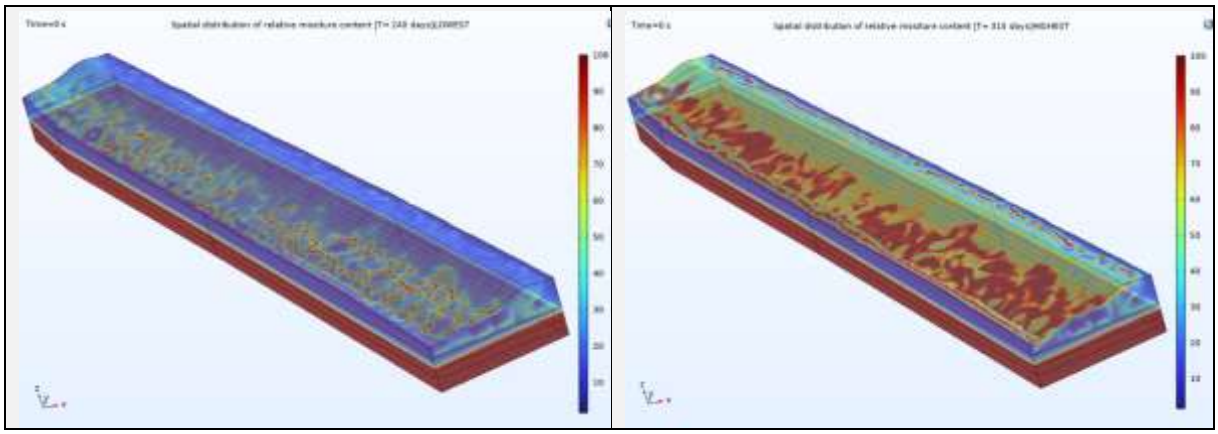

Figure 20 Moisture content distribution for a) Initial condition [t= day 0] b) Average time step [t=day 485] c) Low saturation for drought antecedent period [t=day 240] d) Driest time step [t = day 315]

It illustrates four distinct spatial moisture distributions, enabling observation of the model's initial state, the most average, the driest time step and the wettest time step. Although the model incorporates environmental temperature as an input, it excludes the impacts of evaporation, solar radiation and runoff. To account for these losses, the infiltration along the boundary condition is multiplied by a factor of 0.7 so that 30% of the total rainfall is accounted as loosed in evapotranspiration processes. Moreover, the model was also modified so that when ponding occurs (100% saturation over the surface), the original Dericlect pressure head condition is switched to a Neumman condition of direct flux (Chui and Freyberg 2009). Consequently, all rainfall time series are treated as fully effective infiltrated rainfall within the boundary condition.

To establish the spatial resolution, the spatial derivative for each time step across the entire simulation was computed. The maximum rate of change was then identified for each map. Due to the presence of a preinstalled cable along the longitudinal direction, the derivative was calculated along the model's y-axis, as this axis is expected to exhibit the most significant spatial variation in the cable. The system is configured to ensure the spatial resolution captures the largest area and its variability, with the median value from the time series in Figure 60 selected as the design value. Since the model computes moisture content every 4 hours across 2100 time steps, the median value for the maximum spatial moisture gradient is determined to be 13.75 Sr/m. This result was derived by calculating the time series of the maximum moisture content change in the y-direction, as presented in Figure 19.

4.4. UPDATED MINIMUM SPECIFICATION REQUIRED FOR THE FOS MONITORNG SYSTEM

Based on the results from the updated FEM model after updating the soils hydro-geo-thermal parameters and boundary conditions from the field soil investigations and la results, for the specific case of the dike monitoring system, the update table is presented as:

PARAMETER	VARIABLE	UNIT	DIKE
Measurand minimum frequency (based on 1% Sr moisture content change)	t_θ	sec	139 sec [2.3 min]
Pressure head variation in H2O cm (based on Minimum frequency)	S_θ	m	0.017 [0.17 cm]
Minimal spatial resolution for detecting a 1% Sr change	S_d	m	7.27 cm
Minimum temperature gauge	T_θ	K	±0.061

Table 5 Updated Minimum specification sensing system requirements based on updated FEM

Based on the new results, for the most extreme value changes it seems that the interrogation unit is capable of achieving the required measurement resolution but the maximum change of moisture in space that can be achieved is closer to 2% Sr than 1% as estimated originally as the system is only capable of solving the measurand with a spatial resolution of 20 cm. This is not an important change as the most important feature required for the monitoring system is that can detect fine moisture changes in the vertical direction which will be later used to influence the effective stresses and consequently determining the cross-section slope stability.

4.5. FIELD EXPERIMENT VALIDATION: MOISTURE SENSOR AND DTS VS FEM MODEL

Simulating soil moisture and comparing it with observations from in-situ sensors is essential because point measurements alone cannot fully represent the hydro-physical behavior of a dike when estimated from the DTS. Moisture sensors capture highly local conditions that are influenced by small-scale heterogeneity, installation effects, and depth-specific processes, whereas a finite element model describes moisture evolution as a spatially continuous process governed by physical laws. In normal engineering practice, differences between simulated and observed moisture are therefore expected and can be substantial (in this exercise around 15% of the moisture content), particularly at shallow depths and immediately after rainfall events. While sensors may show abrupt wetting or drying of several percentage points over short time scales, FEM simulations typically reproduce smoother trends because they integrate processes over larger representative volumes and time steps. The present FEM model uses time steps of 4 hours. The importance of simulation lies not in reproducing every short-term fluctuation, but in capturing the dominant moisture dynamics that control dike performance and stability. Some of them can be observed in the long term simulation but the in-situ sensors only have continuous data for 2 different hydrological months.

The dry-month results (August - *Figure 21*) show a coherent behaviour between rainfall, temperature, and moisture. Rainfall events are scarce and of low intensity, and net rainfall is further reduced by the applied evapotranspiration coefficient of 0.7, resulting in limited effective infiltration. Both the measured moisture at different depths and the FEM-simulated moisture at 40 cm exhibit a gradual declining trend, indicating progressive drying of the dike. The lack of pronounced moisture increases following rainfall events suggests that most precipitation is lost to evapotranspiration or remains confined to the near-surface zone. The FEM model captures this slow drying behaviour well, reproducing the seasonal trend and the absence of strong infiltration signals, even though it smooths out the small-scale variability observed in the shallow sensors.

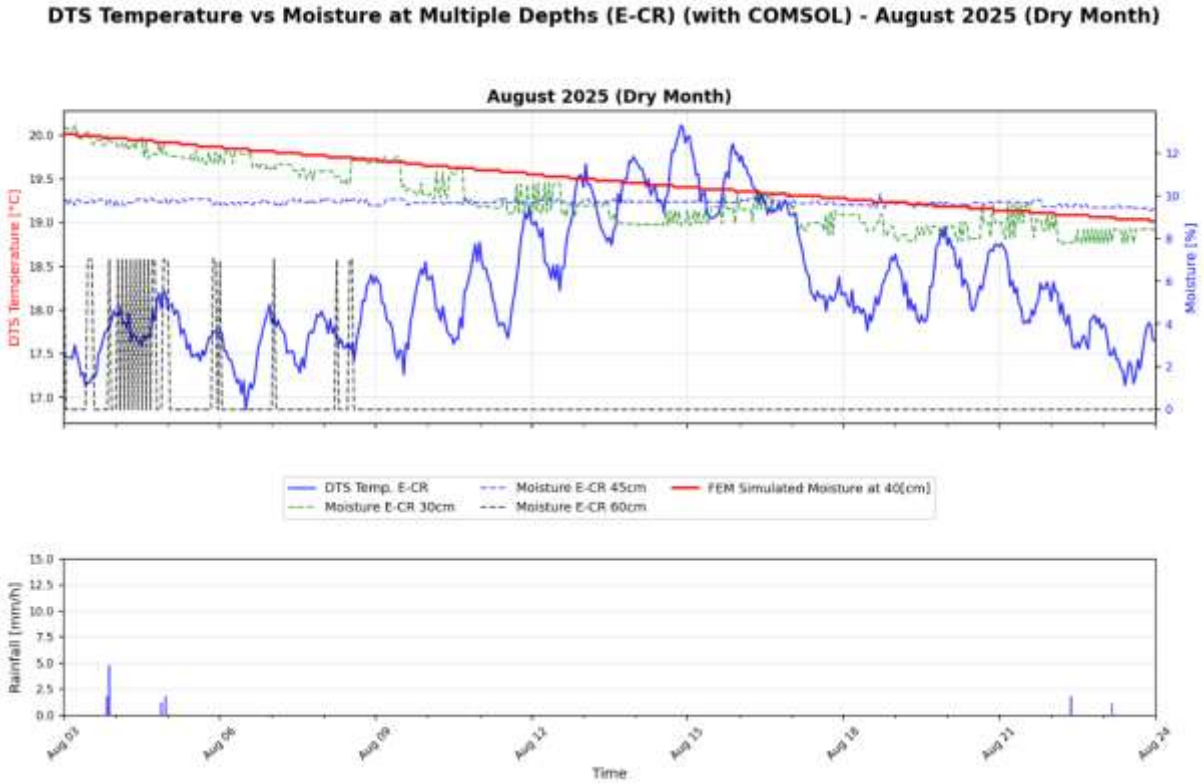

Figure 21 Moisture Sensor vs FEM estimated moisture Dry period.

In contrast, the wet-month results (September - *Figure 22*) clearly reflect the impact of more frequent and intense rainfall events. Periods of increased rainfall correspond to rising moisture levels, particularly at shallow and intermediate depths, while deeper sensors show a delayed and more buffered response. The FEM-simulated moisture follows the overall wetting trend and remains elevated during periods of sustained rainfall, demonstrating the model's ability to capture cumulative infiltration and moisture storage within the dike. However, the simulated response is smoother and less reactive to individual rainfall pulses than the sensor data, especially shortly after rainfall events. This indicates that while the FEM model reliably reproduces the dominant wetting behaviour and moisture persistence, it does not fully capture rapid, localized responses likely driven by near-surface processes or preferential flow paths, which is consistent with expectations in practical hydro-geotechnical modelling.

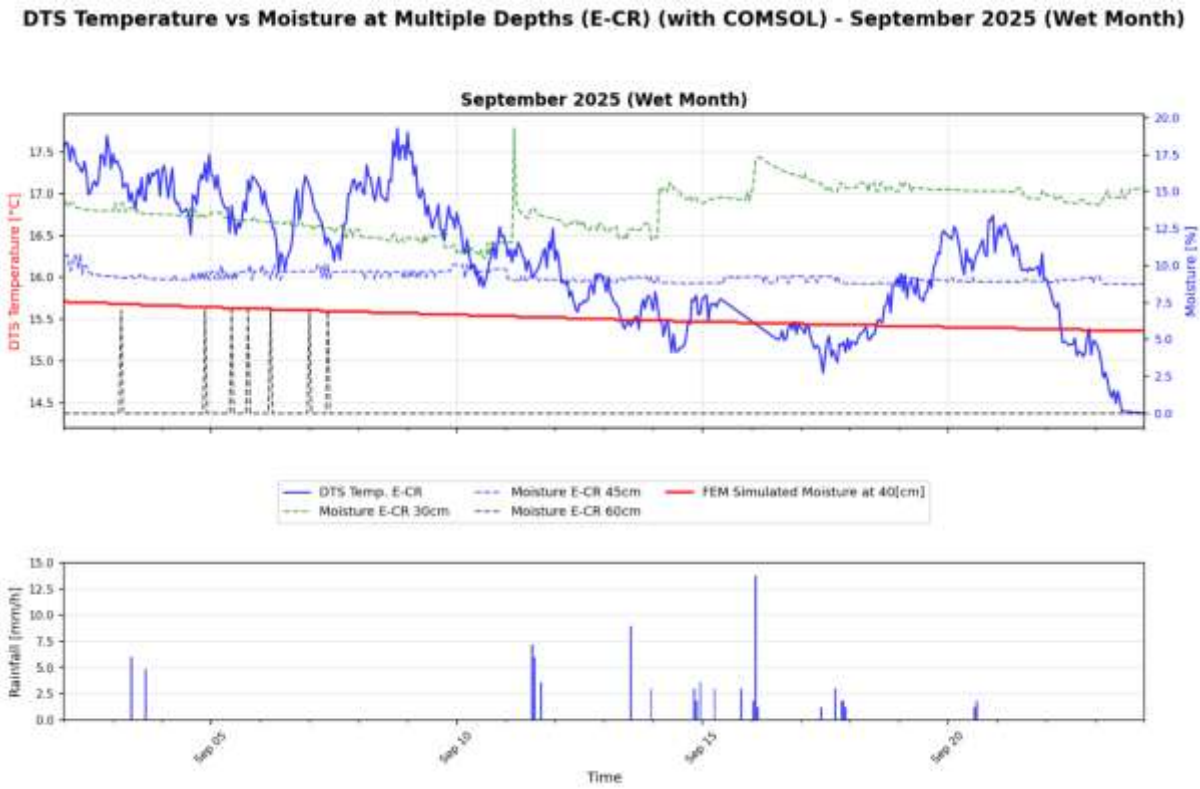

Figure 22 Moisture sensor vs FEM estimated moisture wet period.

The July period results (*Figure 23*) show a mixed hydro-meteorological behaviour that is consistent with early summer conditions. Rainfall events are present but relatively infrequent and mostly isolated, with one more pronounced event around mid-July and smaller events later in the month. As a result, moisture at 30 cm and 45 cm shows a gradual declining trend punctuated by minor increases, indicating that drying dominates but is intermittently interrupted by infiltration. The FEM-simulated moisture at 40 cm initially decreases slightly and then gradually increases toward mid-month, suggesting cumulative infiltration from rainfall that exceeds evapotranspiration over that period. This behaviour indicates that the model is able to capture the balance between rainfall input and atmospheric losses, even when net rainfall is limited. The comparison between observations and simulation also highlights the expected smoothing effect of the FEM model. While the measured moisture at 30 cm exhibits relatively sharp variations and short-lived responses following rainfall, the simulated moisture evolves more smoothly and shows a delayed response. Deeper measurements at 60 cm display minimal variability, confirming strong damping of rainfall signals with depth, which is consistent with the modelled behaviour. Overall, the July results demonstrate that the FEM model captures the dominant moisture dynamics and seasonal transition within the dike, while short-term and depth-specific variability observed by the sensors reflects localized processes that are not fully resolved at the model scale.

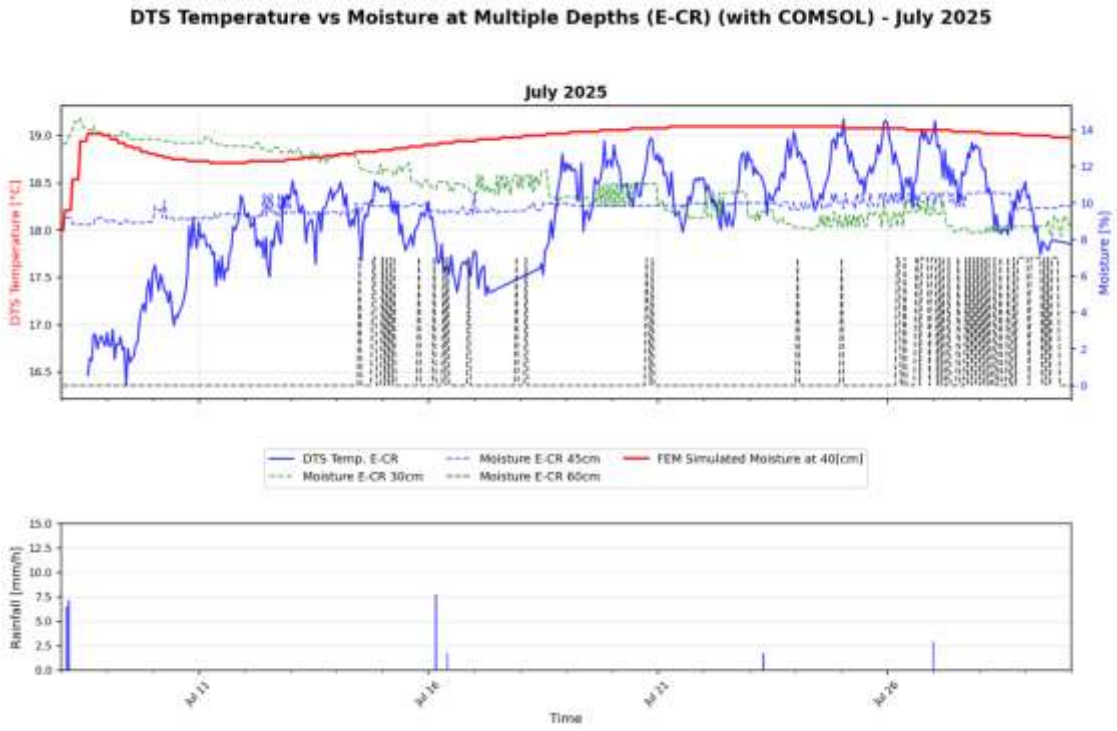

Figure 23 Moisture sensor vs FEM estimated moisture for intense initial rainfall event.

The comparison between simulated and observed moisture suggests that further improvements to the FEM model can be achieved by refining the soil hydraulic parameters, particularly those of the van Genuchten formulation. The gradual trends in the simulations indicate that the model captures the general water retention behaviour, but discrepancies in the timing and magnitude of wetting and drying point to uncertainties in parameters such as the saturated water content (θ_s), residual water content (θ_r), and the shape parameters α and n. In particular, α and n control the steepness of the soil-water retention curve and the sensitivity of moisture to changes in matric potential, and their adjustment could improve the model's ability to reproduce sharper wetting fronts observed in the shallow sensors. Refining the saturated hydraulic conductivity K_{sat} in combination with these parameters would also help better represent infiltration rates following rainfall events.

In addition to parameter refinement, the temporal resolution of the FEM simulations plays a key role in reproducing short-term moisture dynamics. The current time stepping is sufficient to capture seasonal and cumulative trends but is too coarse to resolve rapid moisture changes following intense or short-duration rainfall events. Reducing the time step during periods of rainfall and immediately afterward would allow the model to better represent transient infiltration, redistribution, and near-surface storage processes. This adaptive or event-based time stepping would reduce numerical smoothing and improve the alignment between simulated moisture and sensor observations during critical wetting events.

5. FIBER OPTICS BASED MOVABLE BARRIER MONITORING SYSTEM FINAL CONFIGURATION AND INSTALLATION

This phase of the project was aimed at determining the optimal location of the fiber optic cable over one element of the movable barrier and the design of the cable casing and application to ensure fast installation prior to a flood event. Monitoring the stability of movable barriers is more straightforward as compared to the monitoring the stability of dikes because strain between boxes is directly related to displacement and leakage can be inferred from temperature change. In this section, the calibration of the fiber cable photonic properties and the design of the clamping system used for attaching the cable to the barrier is explained. The testing of the system in controlled conditions is also shown and the resulting recommendations for the eventual final design to be used during the demonstrator is also presented.

5.1. PHYSICAL PRINCIPLE OF OPERATION OF THE MONITORING SYSTEM

To monitor the system performance and detect early signs of displacement or failure, a single-mode optical fiber cable is affixed along the length of the barrier, spanning multiple boxes given the BOFDA nature of the system. The cable is mechanically coupled to the exterior surfaces of adjacent boxes at regular intervals (e.g., at joints or mid-span points) using clamps that work as strain-transfer couplers. Under low loading conditions, the cable experiences minimal tensile or compressive forces. However, when floodwater exerts lateral pressure on the boxes, it induces relative displacement between them—primarily shear or bending—transmitting mechanical strain along the attached fiber cable segments. It is for this reason that the cable is attached with no pre-strained condition and later weights are added in between the boxes (*Figure 24*).

Figure 24 Fibre cable, clamps and pre-strain weights in between box cable connections.

In this manner, the cable will detect strain since the first measurement but when the tension in the cable becomes large, the cable will still have some tension buffer so that it doesn't break. Note that based on the photonic transfer principle of the system, if the cable is broken, the complete system will stop sensing. Strain data is acquired then, continuously along the cable's length at 1-minute intervals using an interrogator unit, enabling real-time mapping of deformation hotspots, barrier deflection, and potential breach risks. This setup allows measurement with thresholds triggering alerts for excessive strain in between boxes (e.g., > 50[με]).

5.2. MECHANICAL STRAIN THEORY APPLIED IN THE SYSTEM

The mechanical behavior of the system/cable is assumed to be well captured by principles of continuum mechanics, specifically the theory of linear elasticity for small deformations and strain transfer mechanics for the sensor integration.

Hydrostatic Loading and Box Deformation:

Floodwater imparts a distributed lateral force on the barrier, modelled as hydrostatic pressure $p = \rho g h$, where ρ is water density (~1000 kg/m^3), g is gravitational acceleration (9.81 m/s^2), and h is water depth. This pressure generates a bending moment M and shear force V on each box, causing localized deflection δ according to Euler-Bernoulli beam theory (*Equation **1***) for the box as a simply supported or cantilever element:

$$\boldsymbol{\delta = \frac{pL^4}{8EI}} \qquad \textit{Equation 1}$$

where L is box span length, E is the effective Young's modulus of the box material, and I is the second moment of area. Inter-box joints experience differential displacement, introducing tensile/compressive strains in connecting elements. The Boxes where modelled as a linear elastic material (Also presented in D3.1) that follows Hook's law of deformation proportionality while assuming a constitutive model based on Young's modulus and Poisson ratio (AB 2019). This choice is supported as it is expected that the material will not be taken to its ultimate state. When the system is in equilibrium, the system of equations ensures that the sum of forces and moments in any part of the material is zero. In the case of presence of external body forces, the system of equations solved for equilibrium are:

$$\boldsymbol{\nabla \cdot \sigma + f = 0} \qquad \textit{Equation 2}$$

where:

- σ is the Cauchy stress tensor [N/m^2].
- f is any external force applied to the system [N].

In this case, the stress-strain constitutive relation is defined for an isotropic linear elastic material by Hooke's laws as:

$$\boldsymbol{\sigma = C * \epsilon} \qquad \textit{Equation 3}$$

where:

- C is the fourth order stiffness tensor [N/m^2].
- ϵ is the strain tensor which is unitless [-].

For isotropic materials, the stiffness tensor C[N/m^2] can be written as *Equation **4*** and represents the stress strain relation:

$$\boldsymbol{\sigma_{ij} = \lambda \delta_{ij} \epsilon_{kk} + 2\mu \epsilon_{ij}} \qquad \textit{Equation 4}$$

For λ and μ which are the Lamé parameters, they can be calculated as a function of the elastic properties of the materials; Young's modulus E [N/m^2] and Poisson's ratio ν [-]. The two terms are expressed as:

$$\boldsymbol{\frac{E\nu}{(1+\nu)(1-2\nu)}}, \boldsymbol{\mu = \frac{E}{2(1+\nu)}} \qquad \textit{Equation 5}$$

For the displacements, the strain-displacement relation used by the softer is expressed as:

$$\epsilon_{ij} = \frac{1}{2}\left(\frac{\partial u_i}{\partial x_j} + \frac{\partial u_j}{\partial x_i}\right) \qquad \textit{Equation 6}$$

By solving this system of equations in 3 dimensions, it is possible to determine the displacements, reacting forces and strain exerted by the material conditioned to a certain geometry. This allows to predict the locations where the largest strain is expected which will consequently determine the position of the fiber optic cable. Note that for this specific case, the interrogation unit is strain based (DSS) as the elongation of the fiber cable is the proxy variable that will be used for monitoring the eventual displacements of the movable barrier.

Strain Transfer to the Fiber Cable:
The optical fiber cable, 300 µm in width with a protective coating is bonded or clamped to the box surfaces with a strain transfer efficiency k (0 < k ≤ 1) deepening on the slipping of the cable quantifies how well the host structure's strain ϵ_h is imparted to the fiber core ϵ_f:

$$\epsilon_f = k\epsilon_h = k\frac{\Delta L}{L} \qquad \textit{Equation 7}$$

where ΔL is the elongation/shortening of a gauge length L along the cable. For perfect bonding (k ≈ 1), the fiber experiences the same axial strain as the substrate. In practice, partial transfer occurs due to coating compliance, modeled via shear lag theory:

$$k = \frac{1 - \cosh(\beta L) + \beta L \sinh(\beta L)}{\beta L \sinh(\beta L) + \cosh(\beta L) - 1} \qquad \textit{equation 8}$$

with $\beta = \sqrt{\frac{2G_s}{E_f r_f \ln(r_s/r_f)}}$, where G_s is substrate shear modulus, E_f is fiber Young's modulus (~72 GPa for silica), r_f and r_s are fiber and substrate radᵢ. Strain accumulates incrementally between attachment points: as boxes displace, the cable segments elongate proportionally, reflecting as peak strains in the collected signal along the cable. The weights may induce Poisson's effect resulting in minor radial strains, but it is expected that axial strain dominates the signal making early detection possible. This mechanical coupling ensures the fiber acts as an embedded "nervous system," with strain gradients revealing wave propagation from pressure fronts.

5.3. FIBER OPTIC CABLE STRAIN CALIBRATION

The main element of the monitoring system is the fiber optic cable used for both sensing and information transmission of the spatially distributed tensions and temperature changes along the barrier. Different manufacturers provide different cable specifications which not only focus on the photonic properties of the glass fiber but also the mechanical and thermal response which varies as a function of the layering and materials used for its construction. As a recommendation from the interrogation unit fabricant (Fibristerre) also partner in the MULTICLIMACT project, a strain sensing taylor-made cable for strain-based applications from the SUCCESS4U company was chosen for the movable barrier monitoring system. The chosen cable is referenced FIBRASENS DSS 2f and it's composed of a double fiber glass core with fiber reinforcement FRP dual element and high-density polystyrene outer squared section jacket as shown in *Figure 25*:

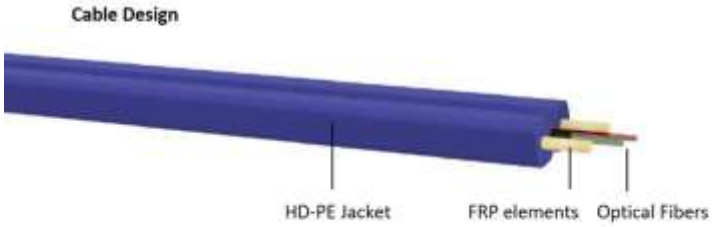

Figure 25 FIBRASESNS DSS 2F strain optimized fiber optics cable used for the movable barrier system

This cable is mechanically compensated so that additional induced strain derived from vending or hanging is reduced as much as possible so that the cable detects mostly axial strain induced stresses. The catalog specifications are present in the following table:

ITEM	REFERENCE	VALUE
Cable Dimensions	-	3.1 mm x 1.9 mm
Cable Weight	-	9 kg/km
Crush Resistance	IEC 60794-1-21 E3	Short Term "X" 1'000N/100mm Short Term "Y" 2'200N/100mm Long Term "X" 500N/100mm Long Term "Y" 1'000N/100mm
Minimum bending radius	IEC 60794-1-21 E11	20 times cable diameter
Tensile load	IEC 60794-1-21 E1	200 N
Outer Jacket	-	HD-PE color Blue
Material spec	2011/65/EU (RoHS 2)	Compliant
Glass fiber type	-	Single Mode G.657A1 Optical attenuation @ 1150nm<0.25 db/km
Temperature exposure range	IEC 60794-2-10	[-20 to 70] degrees Celsius

Table 6 Strain fiber optics cable specifications provided by manufacturer

While the cable standards can be assumed along the complete cable stretch with almost no variation, the signal retrieval calibration depend on the interrogator's technology and its photonic response. For the case of the Fibristerre interrogator ftB 5020, the Brillouin Optical Domain Frequency Domain Analysis (BOFDA) technology, produces changes in the spectrogram also referred to as measurements of Brillouin Shifts which are linearly related to the exerted strain along the fiber as *equation* ***9***:

$$\boldsymbol{train}[\boldsymbol{\mu\varepsilon}] = \frac{(\boldsymbol{Shift_{cable}} - \boldsymbol{Shift_{@20℃}})[\boldsymbol{MHz}]}{\boldsymbol{Coeff_{\cdot Strain}}[\boldsymbol{MHz}/\boldsymbol{\mu\varepsilon}]} \qquad \textit{equation 9}$$

Where:

- $Shift_{cable}$ is the local Brillouin shift along the cable in [MHz].
- $Shift_{@20℃}$ is the calibration Brillouin shift constant at $20℃$ [MHz] with 0 strain.
- $Coeff_{\cdot Strain}$ the scaling coefficient that relates strain and shift [MHz/με]

- $Strain$ The estimated local strain induced by a tensile event [με].

Based on the previous linear equation, the calibration procedure consists in physically measuring induced strain in the cable in a section longer than 20 cm (minimum spatial resolution) and determine $Shift_{@20°C}$ and $Coeff_{\cdot Strain}$ for which at least 2 measurements are required so that an algebraic solution system is possible to solve. The validation was done under controlled temperature and surface leveled conditions in the lab as shown in Figure 26:

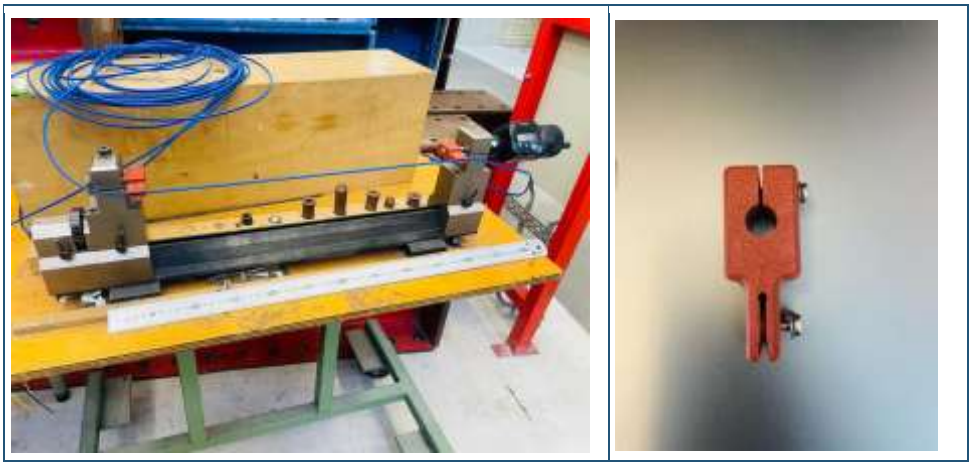

Figure 26 Strain gauge measurements for calibration of the cable

For the present system, the 2 required coefficients were estimated in the past by Fibristerre and validated with few measurements for which a strain gauge meter is used to induce a well-known strain set of values and at the same time, the Brillouin shift is simultaneously recorded. The recommended constats where $Coeff_{\cdot Strain}$ = 46.36 MHz/1000με and $Shift_{@20°C}$ = 10.845 GHz and the test was done by increments of 200 με. It's important to note that the working frequency shift window and the step size resolution are also parameters which require to be calibrated for each set-up but they depend on the amount of strain induced in the cable. For the present calibration, a strain window ranging from 10.85 to 11.00 GHz and the results of the lab points against the suggested coefficients are presented below (Figure 27):

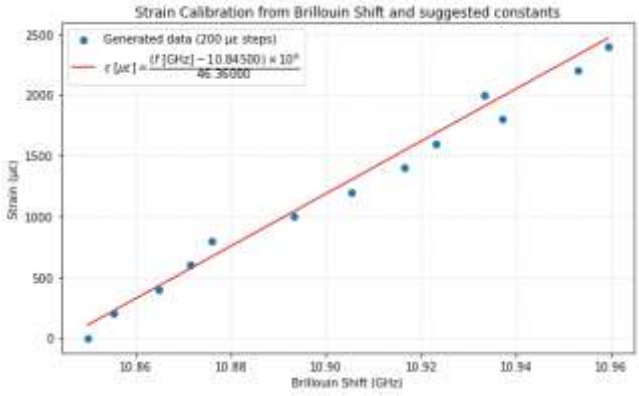

Figure 27 Measured strain and Brillouin shift vs calibration coefficients suggested by Fibristerre.

As it can be observed in Figure 27, the points align with the recommended coefficients in a linear manner. It is also expected that the deviations are explained due to poor coupling between the cable and the lab clamps due to low friction and small surface are between the materials but in an overall, the suggested coefficients are accepted and are to be used for further studies where the same interrogator and cable are used as monitoring system.

5.4. DESIGN OF CABLE ATTACHMENT TO BOX BARRIERS

Three different cable coupling designs where designed, 3D-printed and tested as the good coupling of the fiber optics cable is of paramount importance to detect different type of movement in any of the box barrier elements. Each of the designs correspond to an improved version of the earlier one in terms of its mechanical resistance, installation complexity and grip capacity. Different clamp designs were made and tested in the lab to determine the maximum strains they can withstand before failure and to also test how practical the installation process and times it can take to install them on ground as early as possible with respect to the flood event arrival to the movable barrier.

5.4.1. CLAMP DESIGN V1.0

The first design was conceptualized based on the observations of a temporary clamp 3D printed in the lab for the cable calibration (Orange clamp in Figure 26). During the cable calibration exercise, it was observed that the clamp required to:

- Exert additional pressure to the cable besides the one obtained from the two screws.
- The clamp pressing elements required extra space in the bottom to allow higher bending.
- The length of the cable contact surface had to be increased to increase friction and reduce chances of slipping.
- The bottom surface had to big as big as possible with respect to the design of the Box barrier so that the bending of the clamp does not induce a piercing force in the wall where it should be installed.
- During calibration, strain was induced but it did not tell anything direction about the tensile force that the clap could resist before slipping of getting eroded so it's also important to estimate the strength of grip in by using the actual cable in the design.
- The clamp opening must be printed inclined so that inserting the cable towards the squared cable groove can be done easier and faster.

With these characteristics in mind, a first version of the clamp elements was designed and 3D printed in polylactic acid resin with an average Young Modulus of 3500 [MPa], a tensile resistance of 65 [MPa] and a strain elongation limit 70e3 με. The design has a base of 7.5 cm x 7.5 cm of area of contact between clamp and BOXBARRIER with 4 screw holes in the base and 2 smaller ones in the clamping zone located in the front extension length of 5.0 cm. Based on the cable described in *Table 6*, the clamp is designed with an horizontal grove in one of the clamping sides 3.1 mm X1.7 mm so that when the closing screws are tightened, a compressive force is transmitted to the elastic cable jacket as shown in *Figure 28*:

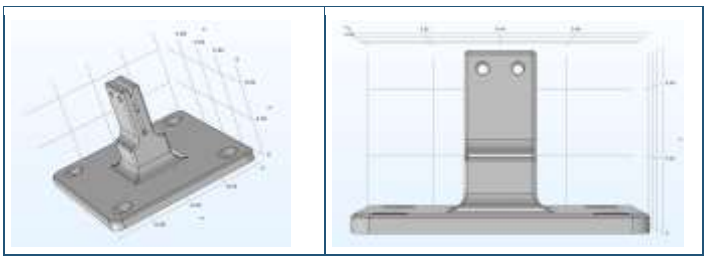

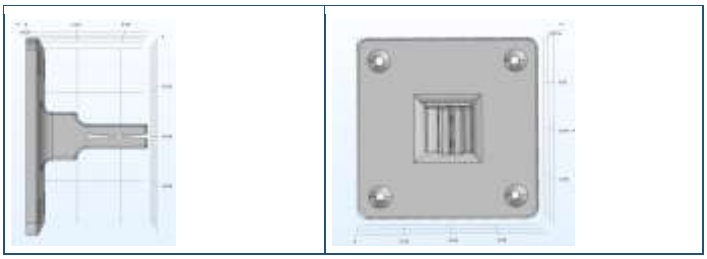

Figure 28 Isometric and different plane views of clamp V1.0 design for 3D printing

Based on this first design, A two simple loading tests were performed as a sensitivity analysis of the response of the cable and clamp to loading with the aim of determining if the cable will resist a large load without developing a brittle type of failure. At the same time, we tested what loading resistance will the clamp resist in case of failing by a slipping condition. To do this, a piece of wood was used as a surface to attach the clamps, and the cable was inserted and compressed with screws in-side the clamps. Afterwards, different loading increments of 1 [kg] were applied to the cable in an horizontal setting and a vertical one as showed in Figure 29:

Figure 29 Vertical test, Horizontal test and loading plates of the clamp tests V1.0.

5.4.2. CONTROLLED HORIZONTAL AND VERTICAL SENSOR TESTS

5.4.2.1. Vertical test measurements:

The experiments were performed based on increments of 1 kg but the system requires to be pre-strained. This allows to analyse the data using the first strain measurement as a reference and later subtracting is from each measurement so that the strain increment is determined. In addition, the double ended nature of the fiber cable setup results in an analogous “mirrored” signal which in its raw format loos like the one presented next:

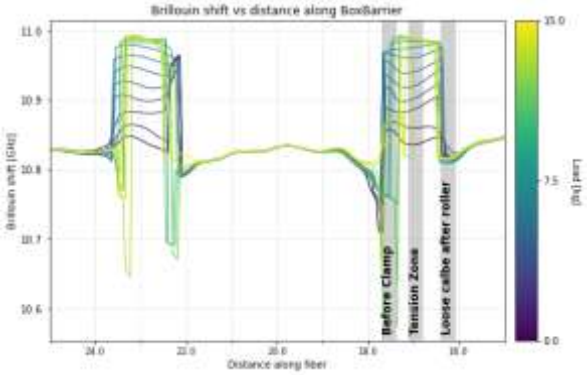

Figure 30 Raw double ended signal of vertical test Clamp V1.0 without using base reference

The raw signal is already subtracted from the base line measurement and therefore it can be observed how the first time-step (16:49:37) is a flat line with 0 strain. The plot also shows how the response of the system is non-linear due to the elasto-plastic nature of the fiber cable which results in smaller strain increments in the latest loading measurements when compared to the earlier ones. The fibrisTerre DSS/DTS interrogator solves strain events with a spatial resolution of 0.2 m. It can be observed in the raw signal (Figure 30) that the strain event recorded for the vertical test is about 1.2 m which correspond to the spanning distance between the upper clamp and the lower rolling pin. In the outer part of the event, 2 negative strain events are recorded. This is expected due to the compression of the cable jacket which induces negative compressive stresses in the fiber before the clamped cable zone. This becomes significantly more evident when the double ended signal is pre-processed by finding the measurement midpoint (end of the cable /end splicing point), inverting one of the signals and averaging in space. This process is known as mirror averaging of the signal and the result in presented in Figure 31.

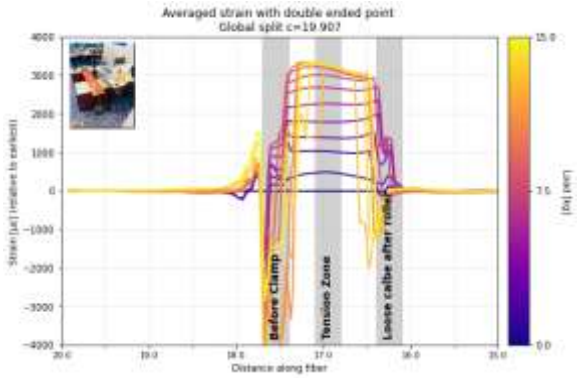

Figure 31 Mirrored averaged signal from the double ended strain measurement

Double ended measurements are required for optimal BOFDA interrogators as the signal is improved by collecting the backscattering signal in two directions as both ends of the cable are plugged to the interrogator which allows to send the signal at one per each of the end points. Based on the spatially distributed nature of the system, it is possible to withdraw the strain measurement by either choosing a point along the cable or by averaging the signal along a certain length span. For this vertical test, three different length spans were chosen and shaded in *Figure 31*; Before the clamp, after the clamp in the tension zone and after the roller pin. Along each of these zones, the signal averaging is estimated for each of the incremental loadings and the results are presented in *Figure 32*.

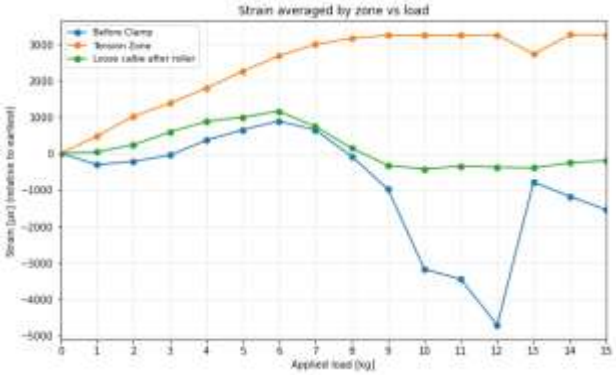

Figure 32 Strain measurement in the averaging zones of the raw signal.

The results show that the cable can withstand a fully tensile loading higher than 15 kgs without breaking but the clamp will start slipping after 12 kgs (orange line). This was concluded after noticing that the incremental load registered a decrease in strain in the tension zone (orange line in *Figure 32*). Moreover, it can be also observed how the cable jacket influences the signal in the zone before the clamp only after 6[kg] where a decrease of strain is early recorded which corresponds to the start of the slipping process (green line in *Figure 32*). This means that the clamp will start losing grip around 2000 με. Note that the compression of the jacket may also happen at the same time as the fiber slides internally whereas that complete slipping from the cable with respect to the walls of the clamp is only registered at 9 [kg]. Note that strain is a relative measurement of elongation of an element. If the element becomes longer in the process, the measured strain becomes lower even with a larger load. This is what is happening once the cable actually slips from the clamp.

5.4.2.2. Horizontal test measurements:

For the horizontal test, the raw signal case, it can be observed how the negative strain before the clamp is also recorded. Note that for this experiment, the cable slipped for a lower final loading and therefore the test was stopped at 11 kg.

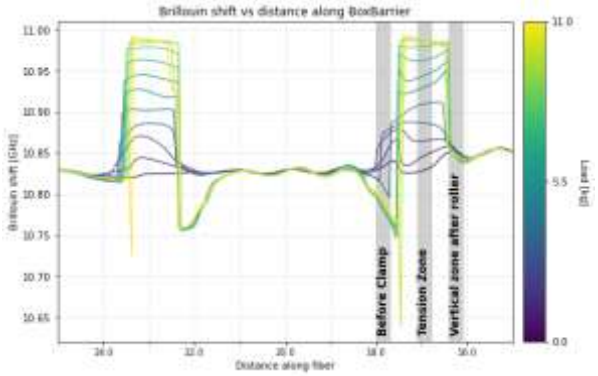

Figure 33 Raw double ended signal of horizontal test Clamp V1.0

After pre-processing the signal, it can be observed that while the cable does not break but the compression of the jacket before the clamp starts influencing the measurement just after 3 kg of tension (see shaded zone before the clamp in *Figure 34* – Mirrored and averaged signal plot). The cable may also present some loss of signal due to the bending along of a narrower bending radius compared

to the allowable one from the manufacturer. This can be observed in the mirrored averaged signal (*Figure 34*) in the shaded zone after the roller.

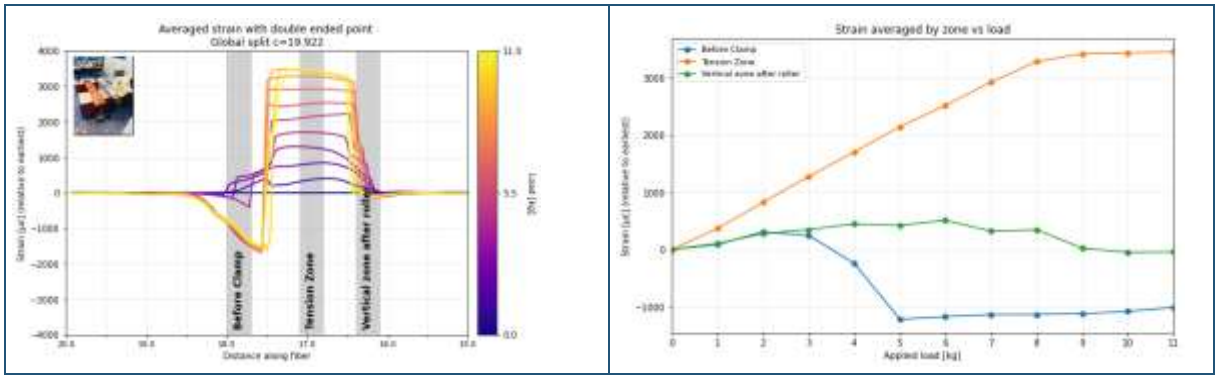

Figure 34 Mirrored pre-processed signal and strain measurement of horizontal test Clamp V1.0

With these results, it was decided that the clamp was good enough for being tested in the field while acknowledging that the tensile force which the loading of the box barrier will break the cable or even break the clamp was still unknown. Moreover, it is expected that the lab test will allow to determine the order of magnitude and range of operation of the system and even further improve the design of the clamp. This knowledge is very important for the operation of the system; especially during a failure flood event for which the movable barrier element may register intra element forces which were not simulated in the original FEM model.

From the FPH controlled experiments it is indented to test:

- The photonic response of the cable based on realistic oblique loading conditions.
- The photonic response of the clamp based on realistic oblique loading conditions.
- The clamp grip behaviour under wet conditions.
- The order of magnitude of the exerted strain, tensile force and cable resistance.

6. FLOOD PROOF HOLLAND LAB TESTS FOR MOVABLE BARRIER (TRL5)

For the movable barrier monitoring system demonstrator, the MULTICLIMACT project aimed at developing and testing a monitoring system that allows to detect displacements of the structural elements of the BoxBarrier flood prevention system by using strain spatially distributed measurements as proxy variables. The tests aim at understanding the coupled behaviour between the monitoring system and the BoxBarrier elements. The BoxBarrier system was developed by the Dutch company "Dutch Water Prevention". As the system is a modular one, it allows to build a temporary flood defense system made from lightweight, UV-stabilized polyethylene boxes, lids, and connecting joints. When empty, the units are compact and easy to stack, transport and store. Their deployment involves placing them end-to-end on any flat surface (no foundation required) along the flood prone area and then filling them with water using a standard pump. The system is intended to be deployed at a speed of 100 m of barrier per hour artificially creating a stable, watertight barrier with a water level retention up to 600 mm high (stackable for greater heights). The water-filled design leverages on the floodwater itself for weight and stability, allowing installation even in partially flooded areas by floating the empty units into place. The hydrostatic pressure is measured by the water level meters behind the barrier. For removal, simply drain the water via pump or gravity, then stack and relocate the lightweight empties. It's fully reusable, recyclable, and effective for dike heightening or temporary dams, A small minis set-up was built to test the water tightness of the system under grass surface conditions at flood proof holland. This proof of concept allowed to determine and accept the BoxBarrier behaviour at the flood proof holland dike lab at TU Delft so that the system testing could be also done here before the actual DEMO. These tests are also important as they will become the proof of concept for a **technology readiness of LEVEL 5** where the development is validated in a relevant environment.

Figure 35 BoxBarrier Movable barrier mini-setup test at Flood Proof holland

The idea behind these tests is to evaluate the performance of the clamp under loading conditions, the fiber cable (sensor) and interrogator all together under transient conditions while monitoring the BoxBarrier movable flood defence system with additional sensors such as water level meters and inclinometers. These tests allow to have controlled conditions and were performed at the dike lab from Delft University of Technology. The experiments were done by installing three clamps V1.0 to the Box Barrier elements, and depending on the experiment, a certain water filling level and flood level on the back basin was done in a controlled manner by operating the basin flooding valves. Based on the strain based working principle of the system, the main idea behind the lab tests is that as the loading speed can be controlled, the reaction capacity and recording frequency time of the monitoring system can be evaluated and fine tunned with respect to the time to first displacement detection and time of failure. As the system will always have an initial strain induced by the clamps, this first

measurement is always used as a baseline. This is an advantage as no pre-strained fixed conditions are required which speeds up the installation process.

During each experiment, two standpipe pressure diver-based water level sensors were installed behind and after the barrier. In addition, a remote thermal camara was installed in front of the barrier on the dry side, to try to detect any major leakage so that later, the cable response at the same time and location can be analysed to see if the system can also detect significant thermal changes.

6.1. EXPERIMENTAL SETUP AT FLOOD PROOF HOLLAND (FPH)

Flood Proof Holland (FPH) is a specialized testing and demonstration facility in the Netherlands, located in a polder near Delft and managed in collaboration with Delft University of Technology (TU Delft). It serves as a semi-full-scale site for developing, evaluating, and showcasing innovative, temporary, modular, and flexible flood defense solutions, such as alternatives to traditional sandbags for urban flood protection. Initiated by the Valorisation Programme Delta Technology & Water (VPdelta), the facility opened in 2013 and focuses on real-world simulations of flood scenarios to improve resilience against rising water levels, including experiments on soil moisture, dyke stability, and mobile barriers like BoxBarrier or Tubebarrier.

Figure 36 Flood Proof Holland (FPH) facility at Delft University of Technology (image taken from Google Earth)

For the MULTICLIMACT project testing phase, 2 different tests were performed in the lower left testing basin (see red circle of *Figure 36*). In this this test basin, a prebuilt barrier can be observed for which the central pools are connected via conduits with control valves so that the inflow can be regulated in time. The idea of the tests is to simulate a transient situation in which the back part of the basin is filled with water meanwhile the BoxBarrier system is installed in the middle so that water cannot pass through (see Figure 37). To achieve full closure inside the testing basin, 11 boxes where water tightly installed from which 4 (A,B,C and D) had clamps installed on them with screws. To each of them, 3 Clamps V1.0 were installed to which the cable is attached and secured by tightening the clamp inner screws to reduce sliding. Two water level meters where installed; one behind and one on front of the barrier so that th hydrostatic pressure difference between the two of them represents the net loading over the barriers.

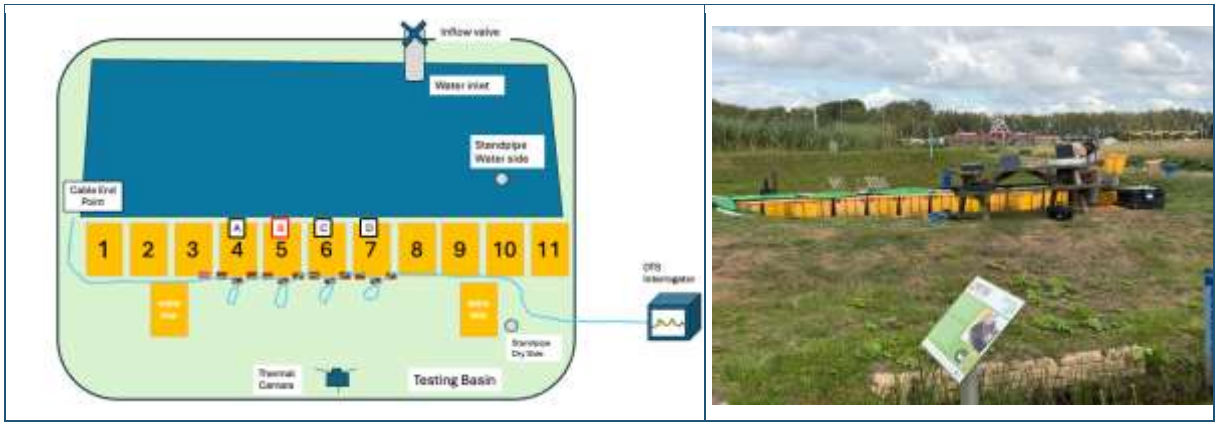

Figure 37 Schematic BoxBarrier FOS monitoring system test experimental set-up inside testing basin

For each test, the Boxbarrier system was monitored by the fiber optics sensing cable attached to the clamps, the interrogator device which process the photonic signal inside the cable and transforms it to strain and temperature in the longitudinal dimension, a thermal camara in front of the barrier to detect large changes of temperature (leakage) and the two stand pipes for water levels. As an additional small test, an extra clamp V1.0 was also installed in box number 3 but instead of using screws, the clamp was glued to the box barrier with a 2-component acrylate based glue to test if this way of installing the clamp could make it easier and faster. This last one, was only done for the last test. For the testing of the monitoring system, two different experiments were proposed and performed to evaluate the performance of the monitoring system:

Experiment 1 (Normal operational conditions): In this test, the idea is to test the monitoring system detection capacity under normal operational conditions (no failure) for which none of the box barrier elements are allowed to fail. To ensure this, all boxes are filled with water to the top filling level, and a green liner is placed over the barrier to ensure a more uniform distribution by reducing the leakage. In this experiment, it is expected to observe and quantify the detection capacity and the sensor and clamp performance under a slow loading.

Experiment 2 (Failure prone condition): In this test, the idea is to test the monitoring system detection capacity abnormal conditions for which one of the box barrier elements is filled only to half of the capacity (32 cm inside Box B; see Figure 37). This means that one of the elements in the barrier is prone to failure due to its reduced weight. It is expected that buoyance and displacement will occur first in that element and therefore the observed failure time is going to be compared to the strain response in time along the sensor. In this experiment, it is expected to observe a significant larger strain in both lateral connections of the partially filled box and the strain response should happen way earlier than in the other boxes.

6.2. BOX BARRIER CABLE CLAMP V1.0 EXPERIMENT 1

The Clamp V1.0 was 3D printed and attached to the BoxBarrier system at three different points per BoxBarrier element (see Figure 38). The original idea intended to measure strain between elements to detect movement and temperature at each element (at the lower clamp) so that later it could be used to infer bottom leakage. Boxes are labelled A, B,C and D and the strain monitoring is done between box coupling which results in strain events between A-B, B-C and C-D in the upper part of the boxes (Figure 38).

Figure 38 Design V1.0 of the clamps attached to the boxes with screws. Three couplings were used per box barrier, two in the top to measure strain and one in the bottom to measure temperature. The picture on the right shows a series of four boxes ready to be used for the experiment

6.2.1. DATA ANALYSIS

The experiment lasted around one hour and 10 minutes and consisted in loading the system from 10 cm initial water depth behind the barrier until 60 cm and then unloading it until 10 cm again. This test will allow to see the response during tension and relaxation. To ensure that there is enough strain capacity, the cable was installed loose and later 250 gr weights are hanged in the connector segments (see Figure 38). In that manner, the cable is pre-strained, but the extra available length of cable ensures that the cable will not be broken during the loading of the BoxBarrier system. The raw signal of the test is presented in Figure 39 as follows:

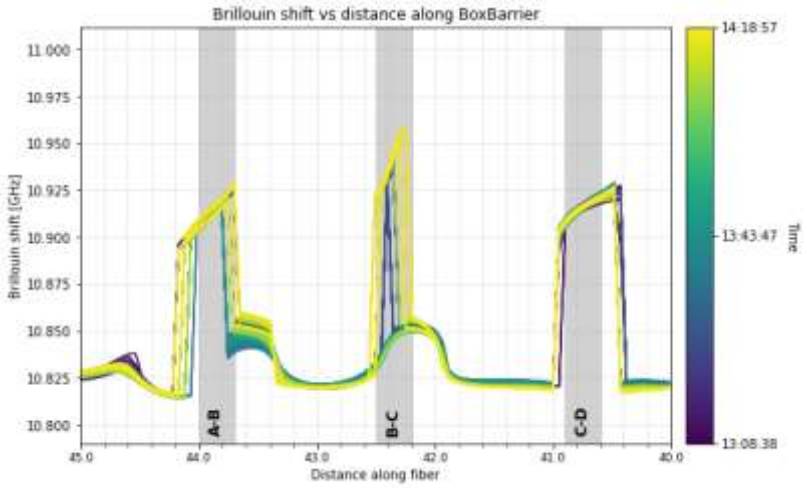

Figure 39 Raw signal of experiment 1. No failure is expected as all boxes are filled to full capacity. The x axis is plotted inverted to make it analogous in space to the connector order shown in Figure 38.

From the raw signal it can already be identified specific zones where the Brillouin shift reported by the interrogator, correspond to the exact location where the strain is induced among boxes. Because BOFDA uses a continuous-wave approach rather than pulses, it is less sensitive to "noise" from the splices at the end point of local breakages of the fiber that were previously fixed. Here, the zero-strain zones observed between connection points (the flat lines between the boxes) are fiber segments likely loose in between same box clamps. It would be interesting to further investigate of the curved zones after the strain events for connections A-B and B-C are induced by the colder

temperature from the cold water in the surface. Based on equation 9 and an averaged value of the Brillouin shift of the shaded sections (25 cm approximately, based on spatial resolution), an estimated strain measurement between boxes is calculated in time and presented as follows in Figure 40:

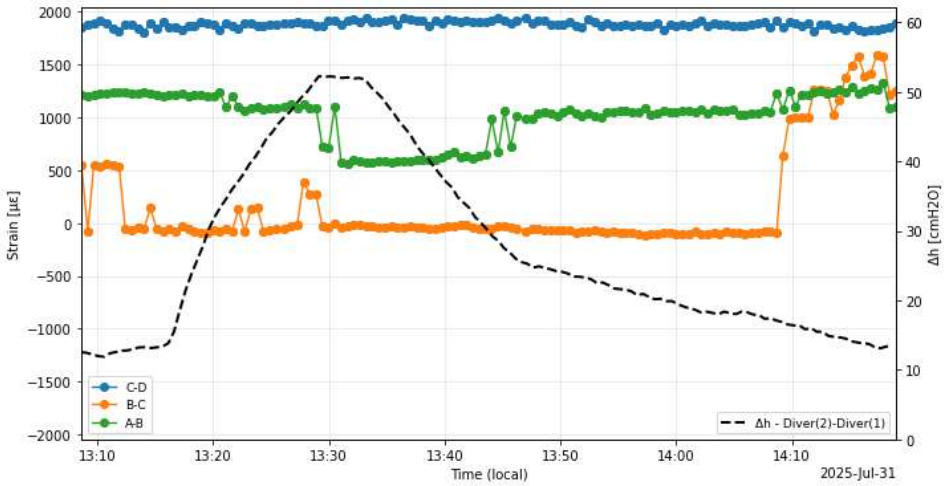

Figure 40 Strain measurement in time of experiment 1. Secondary axis correspond to water level meter behind the barrier plotted as a black dashed line in time.

As a general observation, all connections present a positive strain measurement which demonstrates that all sections are working in tension mode since the start. However, there are few moments in which connection B-C shows small negative values. This is explained by the uncertainty in the choice of the spatial resolution averaging window size and location. Nevertheless, the measurement is consistent to what it was observed during the experiment for which the observed peak in strain around 14:10, was physically induced to test the sensitivity of the system. Yet, besides this event it can be observed how there is only few small movement events around 13:30 where connector B-C gets strained. Boxbarrier system is designed for a maximum loading of 55[cm] which can be observed in Figure 40 at around 52 cm on at 13:19. Based on the topology of the system, connector A-B reduces its pre-strain value which makes sense as box B is sliding from its right corner forward while its left corner remains steady. This is a very interesting finding as it means that it is possible to predict the direction of the failure of each element based on its tensile or relaxing behavior. Overall, it is observed that the photonic response and strain estimation aligned to what is observed during the experiment under normal non-failing conditions. The expected maximum strain under normal operation was around 2000 με while the lab clamp tests resulted in strains around 3000 με before system failure.

6.3. BOX BARRIER CABLE CLAMP V1.0 EXPERIMENT 2

For the second experiment, the idea was to test the system and clamp grip capacity under pre-strained initial state and failure conditions by:

- Filling box B only until 32 cm of water depth. This ensures that at least one of the elements will fail for higher loading. Note that BoxBarrier system is designed for loads of less than 55 cm water depth with a maximum element height of 60 cm.
- Adding equal weights (200 gr) in between boxes so that the cable is pre-strained but with enough “loosened cable” so that when the cable starts getting strained, it doesn’t break earlier in the detection process by inducing too much strain from the failure.

6.3.1. DATA ANALYSIS

The results of the collected raw signal are presented in Figure 41 where the double ended strain measurements during the experiment are plotted. Note that there are 4 signal group pulses at the start of the cable intentionally plotted backwards to reflect the actual topology of the system as the interrogator is connected at the right side of the plot. The BOFDA Fibristerre interrogator is designed and optimized for a "double ended" measurement which basically is 2 parallel glass fibers inside the same cable jacket soldered one to the other in the far end and connected separately to the interrogator. This means that two cables can sense the same point twice. This can be observed as the mirrored behavior where the complete doubled cable is 112 m long with a mirroring point close to 56[m] in the position relative along the fiber. The experiment lasted officially 30 minutes starting at 14:25:51 and finishing at 14:55:53 with measurements every 30 seconds. In this raw signal it can be observed how connection A-B is the one with the largest strain peak given a Brillouin shift close to 11 GHz. Also, it can be observed how the strain event becomes wider as well. This is explained by the fact that the cable is not completely straight in between the clamps. This effect is most evident in the connector which is failing (A-B).

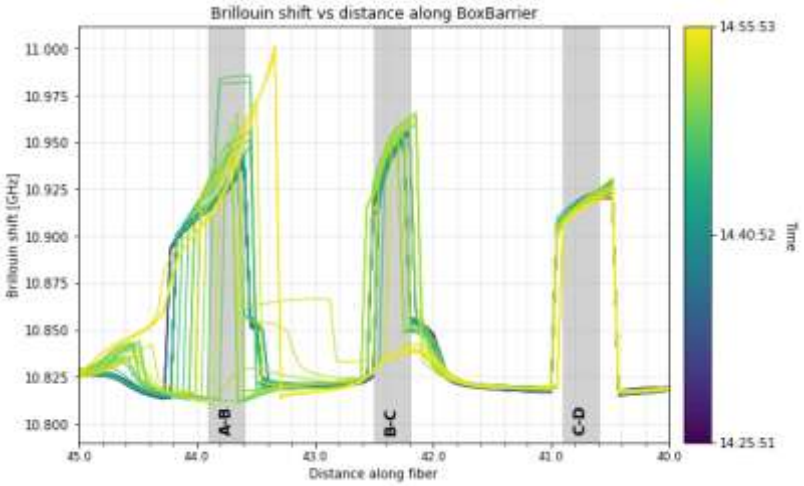

Figure 41 Raw signal along double ended single mode strain compensated cable of the test number 2 at FPH

The results after postprocessing and mirroring average of the signal are presented in Figure 42. Here it can be observed how the strain measurement ranges values between -890 με and 3000 με. These orders of magnitude where expected since the start of the experiment so it seems the system is well calibrated with respect to the calibration equation presented in *Figure 27*. The negative values explanation lays in the fact that the moment the cable slips from the clamp, the actual length of cable between clamps increases "relaxing" the cable recorded actual strain with respect to the base line pre-strained measurement.

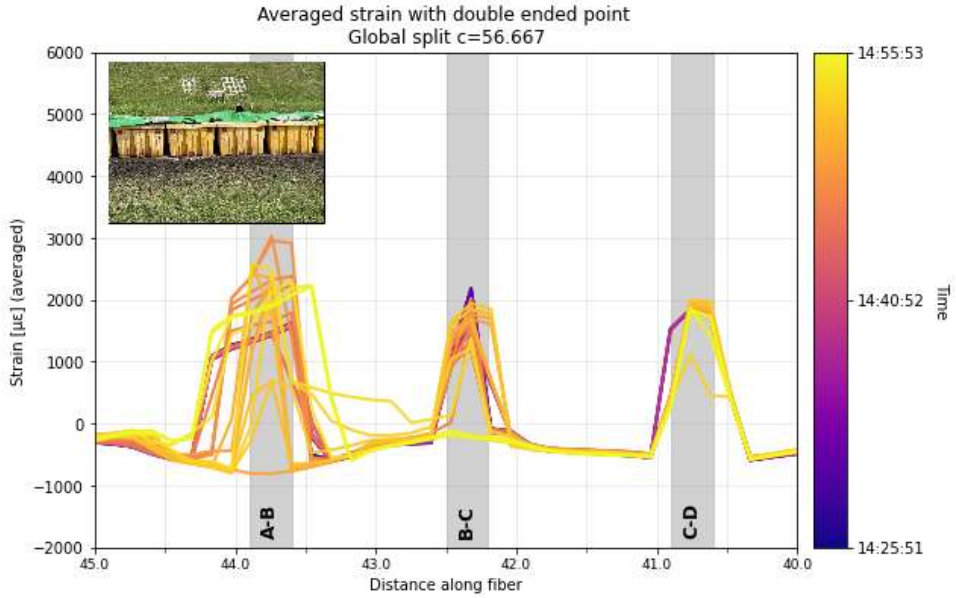

Figure 42 post-processed strain measurements along the averaged fiber.
Picture of setup in the left upper corner show the monitored connection location.

While the cable is Taylor built for specifically problems of strain gauging by being compensated with the FRP elements (see *Figure 25*), it may still detect changes in temperature. This is concluded from the recorded strain between the connector zones (in gray in Figure 42) where additional strain events are recorded between A-B and B-C. Yet these changes are not reliable as they depend on the actual temperature difference between environment and water. Moreover, it can also be observed that the recorded event in these zones is always positive which is expected in case the water is warmer with respect to the environmental outside temperature. Still, is clear from the experiment results that these zones where extra lengths of cable left on purpose in the bottom of each box to detect water leakage do not react as they would with an optimal temperature sensitive cable. It's important to clarify that while these events are recorded as strain in the figure, they correspond to Brillouin shifts used as input in the calibration equation presented in 5.3. which is purely fitted for strain prediction. However, it would be interesting for the next phase of MULTICLIMACT operation phase to calibrate the same cable but for temperature prediction while acknowledging that this cable is not made for that purpose.

The final strain results per connector zone in time are presented in Figure 43. In this one it can be observed how the failure time (14:45:31) is also registered in the green line as a sudden increase in strain. Note that at that same moment, the water loading is around 47 cm which is 14 cm higher than the expected failure load which is equal to the 32 cm inner filling. It was expected that buoyance type of failure will occur at this height, but the green liner placed behind the barrier for water tightness added extra weight to the box and reduce the leakage in the bottom contact significantly. This liner was installed due to the expected leakage beneath the boxes and the grass surface but is not part of the BoxBarrier system.

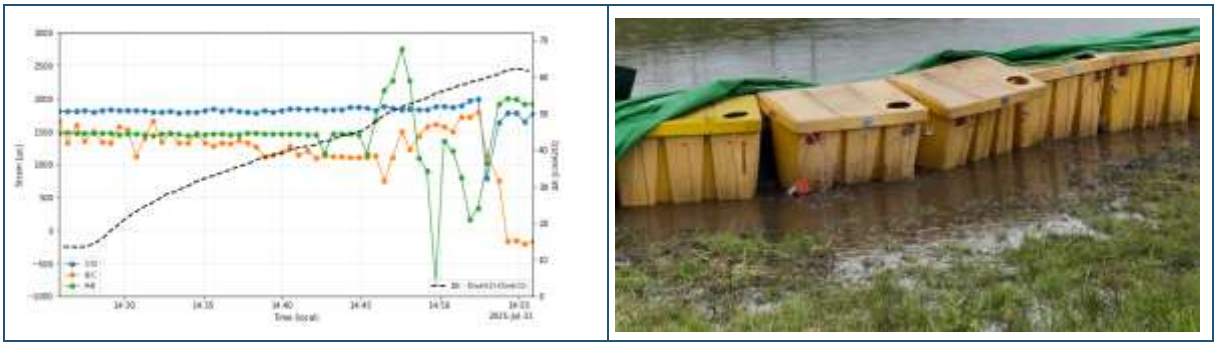

Figure 43 post-processed strain measurements along the averaged fiber.
Picture of setup in the right shows the system in failure.

In the case of connector B-C it can also be concluded that the movement of the B box was both in the forward direction as both side connections present a positive strain measurement. In the case where the A-B connecter has a sudden decrease to negative strain, it means that the clamp failed around 2900 με. Moreover, this same behavior is observed in the other two connectors where the clamps failed between 1700 με and 2000 με.

This first version of the clamp and its behavior in combination with the boxbarrier and the fiber optic sensor was tested in controlled conditions at the flood proof holland basin. Based on the results from these lab loading tests and the performance during the controlled conditions test of the monitoring system, it was concluded that:

- The grip capacity of the clamp was not sufficient so it requires a redesign for which the surface contact area must be increased to obtain a more stable grip.
- The material density used in the 3D printing must be increased as during the installation of the base and clamping screws, it got eroded very easily.
- The Allen/socket groove screws require too much time to be tightened so new screws with either Phillips or flathead type of groove are to be included.
- The temperature measurement as leakage proxy is not possible with the actual cable due to its mechanical compensation for thermal retraction or expansion.
- The fiber optic sensor react almost immediately to the strain events induced to the boxbarrier system. This was validated visually and based on the expected failure height on the strain in time analysis.
- The tensile and compressive nature of the readings may be used to determine the type of failure and tilting direction of each box barrier elements.

7. ADDITIONAL SENSORS

7.1. INCLINOMETER

During the box barrier experiment at FPH, additional conventional sensors were installed with the objective of supporting and validating the observations obtained from the distributed fiber-optic monitoring system. An inclinometer and a thermal camera were deployed to investigate their potential contribution to the detection and interpretation of deformation and leakage phenomena between adjacent box barrier elements. An inclinometer was installed in situ in one of the dikes used for confining the water loading behind the BoxBarrier. These was done the aim of registering potential rotations or relative movements during the controlled hydraulic loading in the levees so that the same type of sensor may be installed in the Tedingerbroek polder dike. It was expected that by the high water loading and the smaller size of the dike compared to the actual demo, large displacement or rotations of the dike could be read. However, during the experiment no measurable inclination or displacement was actually recorded. This outcome is attributed primarily to the lack of a stable external reference point for the inclinometer installation, combined with the limited magnitude of deformation induced under the experimental conditions. As a result, the inclinometer signal remained within the noise level of the sensor throughout the test duration. Although no quantitative deformation data could be obtained, this observation confirms that, under the tested loading scenario, the surrounding dike did not experience detectable rigid-body movements at the scale measurable by the installed inclinometer. The sensor was tested by inducing three consecutive flooding events behind the levee (three different loading experiments of the box barrier) which did not result in a significant and measurable deformation of the levee as shown by the inclinometer (see *Figure 44*).

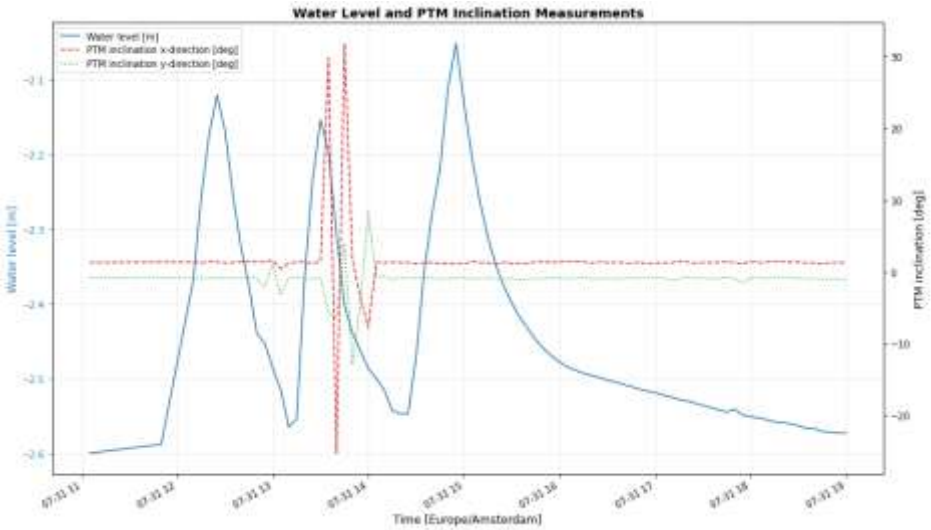

Figure 44 Inclinometer signal from 3 consecutive flooding events.

Although the water level in the basin increased in several well-defined stages, the inclination measurements in both horizontal directions remained largely constant and did not show a gradual or sustained response correlated with the hydraulic loading. Short-duration spikes observed in the inclination signals occurred only during the filling phase and were not physically consistent with expected levee deformation, indicating that they are most likely measurement artifacts related to sensor disturbance, installation effects, or local movement of the sensor mount rather than structural response. In case the levee presented actual deformation or displacement, the tilting signal should

be gradual and following the trend of the water loading. However, the absence of a monotonic or persistent change in inclination suggests that either the induced deformation was below the detection limit of the instrument or that the inclinometer was insufficiently coupled to the levee body, resulting in a lack of correlation between water level variations and measured inclination. Hence is concluded that the installation of inclinometers in the demo site will not give any added value to the safety as this type of sensors will only react by either large flood events or very soft soils.

7.2. THERMAL CAMARAS FOR LEAKAGE

The increasing use of temporary and movable flood protection systems requires monitoring solutions that are rapid to deploy, spatially continuous, and capable of detecting early-stage failure mechanisms such as leakage and deformation. Conventional point sensors provide valuable local information but may fail to capture the spatial extent and evolution of water seepage, particularly in emergency installations. Thermal imaging was employed to explore the feasibility of detecting leakage between and below box barrier elements based on temperature contrasts. A HIKMICRO Pocket 2 handheld thermal camera was used to monitor the surface temperature distribution along the barrier joints during water loading. The underlying assumption was that leakage paths could potentially be identified through localized temperature anomalies caused by flowing water. For this reason, a thermal camera–based leakage detection system code in pyhton was developed as a complementary, non-contact monitoring technique, fully aligned with the objectives with the monistoring system developed for the Netherlands demo site. The method exploits the physical principle that leaking water induces localised surface cooling, creating distinct thermal signatures that can be observed as coherent cold regions on the barrier surface.

The implemented algorithm processes thermal video acquired during hydraulic loading tests of a movable flood barrier. First, all video frames are normalised to a common temperature scale to correct for automatic camera rescaling and ensure that temporal changes reflect true thermal variations rather than imaging artefacts. A stable baseline temperature field is then computed from the initial frames prior to significant loading. Subsequent frames are compared against this baseline to derive pixel-wise temperature changes, with particular focus on areas that become colder over time. Potential leakage zones are identified using adaptive percentile-based thresholding, which allows robust detection under varying environmental conditions without requiring absolute temperature calibration. To reduce false detections caused by textured or heterogeneous surfaces, the method applies a spatial uniformity filter, exploiting the fact that water-covered areas exhibit low thermal variance compared to surrounding materials. Morphological operations are then used to remove noise, enforce spatial coherence, and optionally expand detected regions to capture the full leakage footprint. The analysis is restricted to a predefined region of interest, typically the lower part of the barrier where hydrostatic pressure is highest. The result is a time-resolved map of leakage occurrence and extent, which can be visualised in real time and quantitatively assessed as a fraction of the monitored area.

By combining physical temperature change detection with spatial and temporal filtering, the thermal camera system provides a robust, non-invasive means of leakage identification. When integrated with fiber-optic sensing and other in-situ measurements, it enhances redundancy, supports cross-validation, and improves confidence in early-warning capabilities for movable flood defence systems.

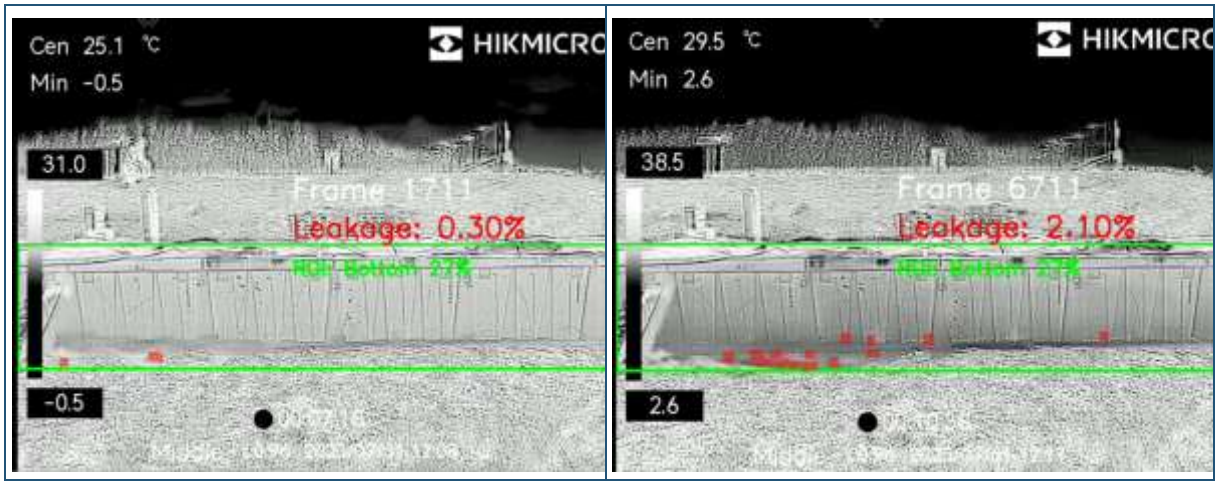

Figure 45 Initial "dry" and "wet" states video processing detection of experiment at fph

The two thermal frames in Figure 45 represent distinct loading states of the testing experiment of the movable BoxBarrier at flood proof holland: **(i) a pre-leakage reference condition** and **(ii) an active leakage condition**. Both frames are processed using identical parameters, including temperature normalization, region-of-interest (ROI – Green box) restriction, uniformity filtering, and adaptive thresholding, allowing a consistent comparison.

Pre-leakage frame (Frame ~1711, Leakage ≈ 0.30%)

In the first frame, the thermal field along the barrier toe appears **spatially heterogeneous**, with no dominant cold anomalies. Within the defined ROI (bottom 27% of the image, highlighted in green), only a **very small number of isolated pixels** are detected as colder than the baseline. These detections are sparse, discontinuous, and remain below the configured minimum-area and spatial-coherence thresholds. As a result, the computed leakage indicator remains low (≈0.30%), consistent with **background noise**, minor thermal fluctuations, or local surface effects rather than hydraulic seepage. Importantly, the detected cold pixels do not form spatially uniform regions, which confirms that the **uniformity filter successfully suppresses false positives** caused by textured ground or material interfaces.

Post-leakage frame (Frame ~6711, Leakage ≈ 2.10%)

In contrast, the second frame shows **multiple spatially coherent cold regions** along the lower interface of the barrier. These regions are clearly confined within the ROI and are characterised by:

- Lower apparent temperature relative to the baseline,
- High spatial uniformity, consistent with water-covered surfaces,
- Clustering and lateral continuity, indicative of seepage rather than point noise.

After baseline differencing, these areas exceed the adaptive percentile-based temperature threshold and survive the morphological filtering and minimum-area criteria. The algorithm therefore classifies them as leakage-related cold spots. The resulting leakage percentage (≈2.10%) reflects a **clear increase in the fraction of the barrier base affected by cooling**, which is physically consistent with the onset and propagation of water leakage under sustained hydraulic loading.

Detection process validation

The comparison between the two frames demonstrates that the detection pipeline correctly distinguishes between:

- Pre-leakage conditions, dominated by random, non-uniform thermal variability, and
- Active leakage conditions, characterised by persistent, uniform, and spatially coherent cooling patterns.

The restriction to the bottom ROI (green box) ensures physical relevance (hydrostatic pressure zone), while the uniformity-based filtering removes false detections from grass, soil texture, and structural details. The leakage metric derived from the detected pixel area provides a **quantitative and time-resolved indicator** of barrier performance degradation.

8. FINAL SENSOR DESIGN READY FOR LIMBURG DEMO

8.1. CLAMP DESIGN V2.0

Based on the lessons learned in the lab and FPH tests of the monitoring system and the performance of the clamp V1.0, a new clamp was designed and printed. This design is intended to solely be tested from the mechanical point of view and if approved, will be the final design adopted and implemented for the official demonstrator in Limburg. The new design was optimized by:

- Extending the cable clamp contact area equivalent to the complete base width of the contact zone between clamp and Box barrier element.
- The mid-section of the clamp outer extension was modified from concave to convex so that the rigidity of the mid-section was increased without changing the density of the material which results in a greater pressure transmitted from the clamp to the cable. This will reduce the chances of the cable to slip due to plastic deformations in the clamp.
- An additional screw hole was added to increase the pressure from the clamp to the cable.
- The cable inner groove was moved deeper inside the clamp to better distribute the exerted pressure from the base and the outer screw's part to the cable.
- Due to the modification of the cable square groove location, the inclination of the surface of one of the clamps that allows to insert the cable was also modified.

Based on the previous considerations, the new design is presented in *Figure 46*:

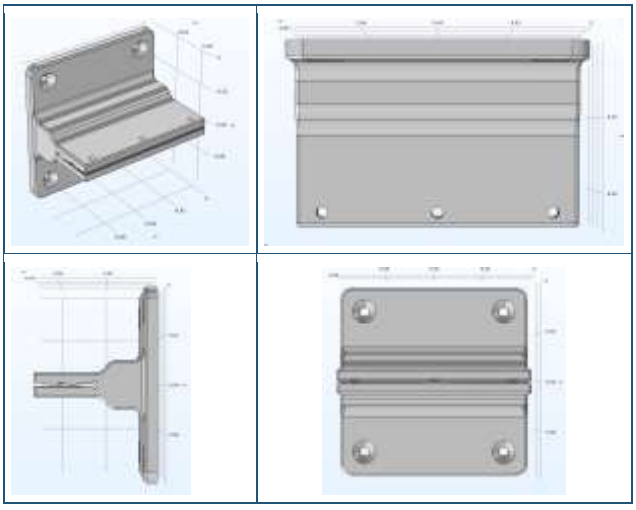

Figure 46 Isometric and different plane views of clamp V2.0 design for 3D printing

To test the mechanical integrity of the clamp, we conducted again a vertical load test using a fiber optic interrogator to measure strain in real-time. Before testing, the clamp was improved by extending the contact area to match the base width, changing the outer extension from concave to convex for increased rigidity, and adding a third screw hole for higher pressure. Additionally, the inner groove was moved deeper for better pressure distribution, and the insertion surface inclination was adjusted. During the test, the strain increased linearly until reaching a peak at 4 kg (see Figure 47), at which point a sharp drop in strain indicated that the clamp failed to hold/grip the cable securely while the cable was exerting a strain a bit above the 2000[με].

8.1.1. DATA ANALYSIS

Following this initial failure and subsequent mechanical settlement, the system stabilized and showed a gradual, linear increase in strain as the load continued up to 13 kg.

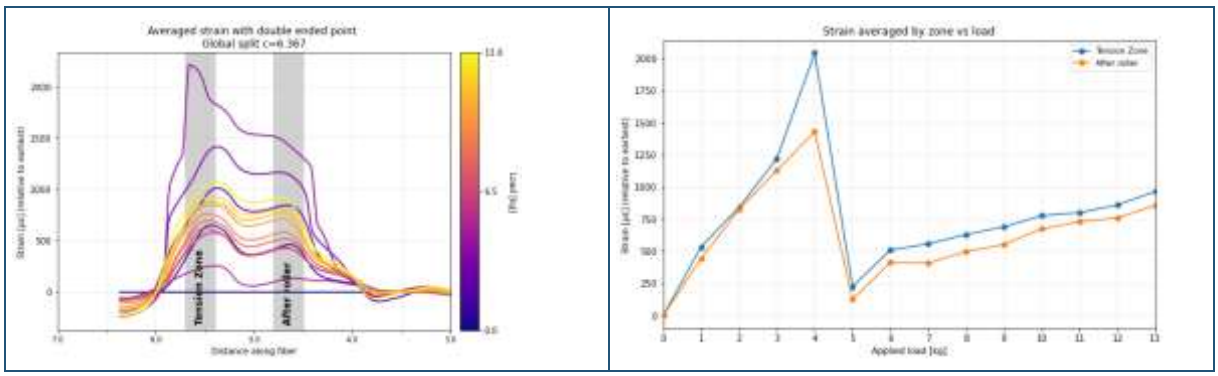

Figure 47 Strain distributed averaged signal and strain measurement per section until 13 kg.

The technical failure observed at the 4 kg load mark was rooted in a pre-existing structural crack over the clamp body. As shown in Figure 48, the extreme pressure exerted by the three tightening screws—intended to secure the cable—caused the 3D-printed material to fracture along the horizontal axis of the mid-section, reducing the grip capacity. This crack originated at the stress concentration points near the screw holes and propagated through the center of the clamp during the loading test. This is concluded as a bigger contact area should have resulted in a higher loading capacity instead of leading to the sudden drop in strain as recorded by the interrogator.

Figure 48 Broken Clamp V2.0 after loading test.

8.2. CLAMP DESIGN V3.0

To address the structural failures and early slippage observed in previous testing, a redesigned clamp was developed and tested again under vertical load testing. The redesign focused on eliminating stress concentrations along the walls to enhance grip reliability and maximize material rigidity against the axial forces exerted by the cable. To achieve this, the last design aimed at:

- Removing the screws and increasing the rigidity of the system so that it becomes a push-in system.
- Increase the inner printed roughness inside the clamp walls to reduce the chances of sliding, especially when in contact with water.
- Changing the orientation for printer inside the 3D printing tray to increase rigidity of the material with respect to the axial forced applied from to the cable.

- Adding extra outer clip rail in case more strength is needed so that a metal clip can be easily slide.

Based on the previous considerations, the new design is presented in Figure 49:

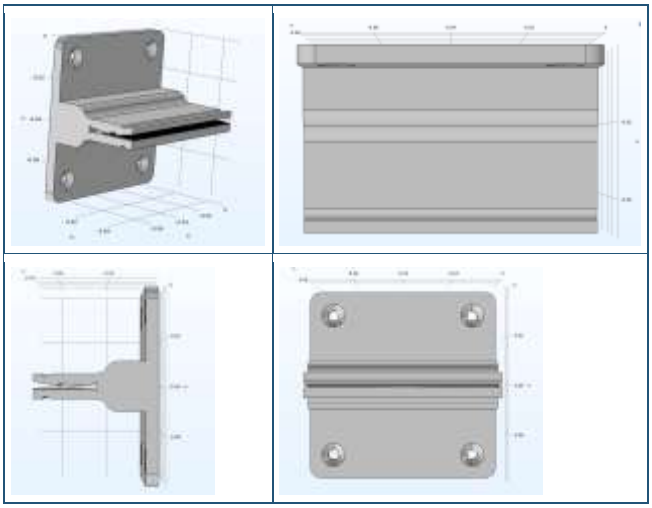

Figure 49 Isometric and different plane views of the final clamp V3.0 design for 3D printing

The performance of this redesigned push-in system is shown in Figure 50, where the "After Clamp" zone exhibited a steady, linear increase in strain throughout the test. Unlike the previous iteration, which fractured under screw pressure, the redesigned clamp maintained its structural integrity perfectly along the whole test. The grip was so effective that the clamp never failed and only increments of strain were recorded inside the tension zone after the clamp; instead, the test reached its limit when the fiber optic cable mechanical resistance was reached and broke under the extreme tension. We also believe that this same cable resisted higher loading in the past before reaching is plastic deformation zone (see Figure 34).

8.2.1. DATA ANALYSIS

As shown in the data, the strain in the "After Clamp" zone continued to climb smoothly, reaching approximately 3500 [με] without any of the sudden drops that characterize slippage inside the clamp.

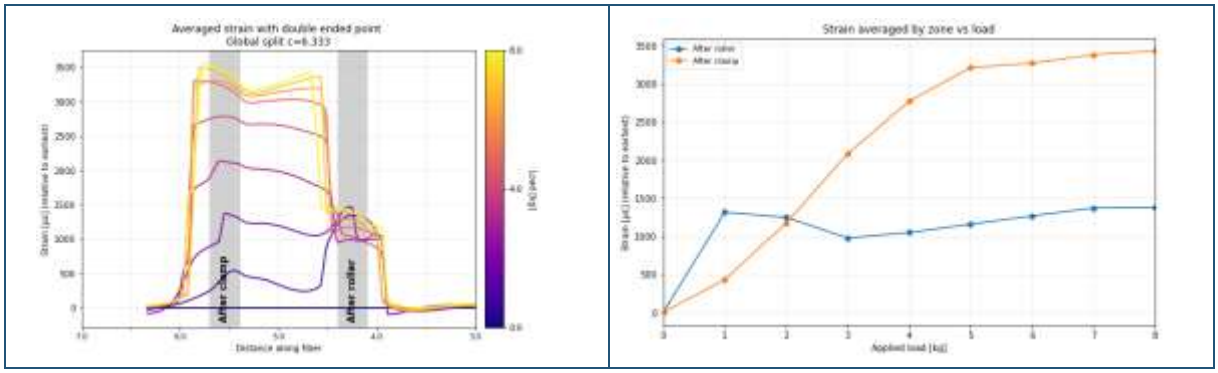

Figure 50 Strain distributed averaged signal and strain measurement per section until 8 kg.

With the final clamp design, the complete fiber optics monitoring system system is now fully prepared for deployment and testing in the upcoming demonstration in Limburg (TRL6), where it will be tested under the extreme and realistic conditions of a simulated flash flood event to monitor the movable barrier in real-time.

9. INTERROGATOR IMPROVEMENTS AND INSTALLATION PROTOCOLS

Within the scope of the project, two major parameters of the fTB 5020 interrogator unit (and, in more general terms, of the Brillouin Optical Frequency Domain Analysis – BOFDA) were envisaged.

9.1. IMPROVEMENT OF THE SPATIAL RESOLUTION OF BOFDA

The spatial resolution is one of the central performance figures of any DFOS system. In general, the following definition has been widely accepted throughout the industry:

- The spatial resolution is specified for a fiber by the minimum distance between two step transitions of the fiber's strain / temperature condition. It is directly related to the pulse length of the measuring instrument.
- For general time-domain DFOS systems, a rectangular pulse of 10 ns length allows a spatial resolution of 1 m.

When considering incoherent frequency-domain systems, such as BOFDA, the pulse length is not directly determinable because no physical pulses are used. In BOFDA, a series of sinusoidally modulated signals is injected into the optical fiber as the pump light; the received signal (the Stokes wave, upon which the sinusoidal modulation is transferred) is analyzed by gain and phase, which – over the full series of different modulation frequencies – results in the complex transfer function, that, eventually, can be converted into the pulse response (and thereby the equivalent time-domain signal of a BOTDA system) by means of an inverse Fourier transform.

Whereas in a time-domain system, the spatial resolution is directly related to the pulse width, in a frequency-domain system it is related to the width of the virtual pulse after the inverse Fourier transform, and therefore, in its origin, determined by the bandwidth (or range of the frequency scan) of the sinusoidal intensity modulation.

In the current BOFDA implementation as in fibrisTerre's interrogator unit fTB 5020, the modulation bandwidth of 100 MHz results in a spatial resolution of 0.5 m.

The current ongoing development within the scope of the project aims to result in a spatial resolution of 0.25 m, which is achievable by increasing the bandwidth of the intensity modulation to 200 MHz

At the time of writing, the increased bandwidth of the BOFDA system on the levels of:

- Analog hardware
- Signal converters (ADC and DAC)
- Electro-optical modulators and photo-receivers
- Embedded system design (FPGA)
- Digital data transmission
- Software analysis

are in the state of prototyping, a first hardware prototype is expected to be available for lab testing in Q2/2026.

Remaining challenges are the physical response of Stimulated Brillouin Scattering to high modulation frequencies. This will remain subject of fundamental research and will govern the actual outcome of this work and its applicability to the ongoing demonstrators.

9.2. IMPROVEMENT OF THE MEASUREMENT SPEED / REPETITION RATE OF THE FTB 5020

Especially for the testing of the Movable Barriers under real-world flooding conditions, the repetition rate of single iterations of the fTB 5020 for distributed strain measurements was improved.

The main development in this regard affects the order of internal operations in the fTB 5020 together with the PC application fTView that configures the strain / temperature measurements, manages the data transfer and performs the top-level analyis.

During the project work, it has been found that significant room for improvement lies in making the internal calibration process in the system more efficient.

While the measurement itself (frequency sweep of the laser-locking system to scan the fiber-optic sensing cable for local maxima of Stimulated Brillouin Scattering) for the given fiber length and strain range is within 25 seconds, the calibration procedure for each iteration adds around 10 seconds to this acquisition time. By elaborating the exact requirement for periodic calibration – other than performing this procedure each time before a measurement iteration – the measurement speed has been improved by around 25% which allowed a higher repetition rate at the field demonstrator tests on the movable barriers in Roermond in October 2025. Further improvement on measurment time are aimed at along with the above described widening of the bandwidth to 200 MHz, mainly for the single-ended variant of the technology (BOFDR).

9.3. INSTALLATION PROTOCOLS

9.3.1. INSTALLATION PROTOCOL FOR THE DIKE MONITORING SYSTEM

The installation of the Distributed Fiber Optic Sensing (DFOS) system for the dike demonstrator was carried out following a structured protocol to ensure reliable temperature measurements, proper soil coupling, and long-term monitoring stability. The installation focused on proper fiber placement, integration with complementary sensors, and secure hardware configuration within the Early Warning System (EWS) architecture.

9.3.1.1. Site preparation and layout design

Prior to installation, the monitoring layout was defined based on the geometry of the dike and the monitoring objectives. The fiber optic cable alignment was selected to cover representative sections of the crest, slope, and toe of the structure to allow detection of thermal anomalies associated with seepage, moisture variations, and structural changes.

The installation route was geo-referenced to allow accurate mapping of the measurements within the monitoring dashboard and GIS environment. Complementary sensors, including volumetric moisture sensors and groundwater pressure sensors, were positioned along the same alignment to provide validation data and improve interpretation reliability.

9.3.1.2. Fiber optic cable installation

The single-mode fiber optic cable was installed along the selected dike section using shallow trenching techniques to ensure good thermal coupling with the surrounding soil while maintaining mechanical protection.

The installation procedure included:

- Marking the cable route according to the monitoring design
- Excavating a shallow trench along the alignment
- Installing the cable while respecting the minimum bending radius
- Careful backfilling using original soil material
- Recording cable coordinates and installation characteristics

Particular attention was given to maintaining consistent burial conditions to avoid measurement artefacts caused by heterogeneous thermal environments. Special care was also required at splice locations and transition points to avoid signal disturbances.

9.3.1.3. Installation of complementary monitoring equipment

To strengthen the monitoring framework, additional sensors were installed to support interpretation of fiber optic measurements. These included moisture sensors, groundwater pressure sensors, and rainfall measurements to provide environmental context to the temperature observations.

All sensors were registered within the system database and integrated into the EWS platform to enable synchronized data collection and analysis.

9.3.1.4. Interrogator installation and system integration

The interrogator unit was installed in a protected indoor location to ensure stable operation and secure connectivity. The installation included connection of the fiber optic cable, configuration of data acquisition software, and integration with the cloud-based monitoring platform.

The system architecture follows a layered approach consisting of the sensor layer, integration layer, and presentation layer, ensuring robust data collection, processing, and visualization.

9.3.1.5. Commissioning and verification

Following installation, verification tests were performed including signal continuity checks, baseline measurements, and validation against reference sensors. These steps ensured proper system functioning before continuous monitoring operations started.

The resulting installation protocol demonstrated that DFOS systems can be effectively deployed for continuous monitoring of flood defence structures when careful attention is given to cable placement, environmental coupling, and system integration.

9.3.2. INSTALLATION PROTOCOL FOR THE MOVABLE BARRIER MONITORING SYSTEM

The installation protocol for the movable flood barrier monitoring system was developed to enable reliable strain monitoring during controlled hydraulic loading experiments. The installation emphasized proper strain transfer between the structure and the fiber optic cable, rapid deployment capability, and reliable data acquisition under dynamic loading conditions.

9.3.2.1. Experimental setup preparation

Due to the temporary and rapidly deployable nature of the movable barrier system, the monitoring setup was designed to allow fast installation while ensuring measurement accuracy. The fiber optic monitoring configuration was aligned with the barrier geometry to capture strain development along the connected barrier units.

Additional instrumentation including water level measurements and thermal imaging was used to complement the strain monitoring and provide additional validation of system behaviour during loading tests.

9.3.2.2. Fiber optic cable installation on the barrier

Unlike the dike installation, the fiber optic cable was directly attached to the structural elements of the movable barrier to enable accurate strain transfer. The installation required careful mechanical attachment to ensure that the measured strain corresponded to structural deformation.

The installation procedure included:

- Positioning the fiber along the barrier alignment

- Securing the cable using mechanical fixtures
- Ensuring proper tension without pre-loading the fiber
- Recording reference measurements prior to loading
- Verifying signal continuity

Special attention was given to connections between barrier units, as these locations were expected to experience higher strain concentrations during hydraulic loading.

9.3.2.3. Calibration and baseline measurements

Prior to the experiments, calibration of the fiber optic sensing parameters was performed to ensure consistency with the Early Warning System requirements. This included determination of strain and temperature coefficients and establishment of baseline conditions before loading tests commenced.

Baseline measurements were essential to distinguish structural response from installation effects and to define reference conditions for early warning thresholds.

9.3.2.4. System integration and testing

Following installation, the monitoring system was connected to the interrogator unit and integrated into the monitoring dashboard. Real-time measurements were verified through test acquisitions to confirm system responsiveness and data quality. The monitoring configuration allowed strain measurements to be updated approximately every 40 seconds, enabling near real-time observation of structural behaviour during the experiments.

9.3.2.5. Commissioning

The system was considered operational after successful verification of signal stability, data transmission, and correspondence between measured strain patterns and expected structural behaviour during initial loading phases. The installation demonstrated that distributed fiber optic sensing can be effectively deployed on movable flood protection systems, providing high-resolution strain monitoring suitable for early warning applications and structural performance assessment.

10. DEVIATIONS TO THE PLAN

Before the start of phase 2 of MULTICLIMACT, it was requested to the coordination and project office to extend the deliverable 9.1 submission 6 months later aligned with deliverable 11.3 instead of doing it in the original second phase milestone of the end of WP9. The main goal of this request was to have a longer period for collecting a larger variety of environmental data and to better prepare the Limburg movable barrier demonstrator which was planned for the later 2025. This not only helped to collect data but helped to coped with some issues in the dike with respect to the power supply of the site. During the implementation of Deliverable D9.1, minor technical deviations from the original plan were encountered due to operational constraints and iterative design requirements. At the dike monitoring site, intermittent electricity shortages and unplanned power cuts limited the continuity of data acquisition over certain periods, resulting in temporary gaps in the monitoring time series. These interruptions were caused by external factors related to site operations and were outside the direct control of the project consortium. However the time extension allowed to easily cope with these delays and finish all work in time and with very good results. Example of mitigation measures were implemented to restore system functionality, and the available datasets remained sufficient to validate the monitoring concepts and system performance .In parallel, additional time was required to converge on the final design of the mechanical clamp for the movable barrier monitoring system. The initial design did not fully account for strain transfer efficiency, mechanical robustness, and rapid deployment constraints, necessitating iterative testing and refinement. While this extended the design phase beyond initial estimates, it resulted in a significantly improved and demonstrator-ready solution. Overall, these deviations had no major impact on the project objectives or progress, and the work remains well aligned with the original project timeline and task results, with the achieved results strengthening the readiness of the monitoring systems for subsequent demonstration and deployment phases.

11. OUTPUTS FOR OTHER WPS

The present Deliverable (D9.1) describes the activities carried out within T9.1. This WP is embedded within a sequence of interrelated work packages and deliverables, acting as a **controlled experimental validation step** between sensing system specification, modelling activities, and demonstrator-scale implementation.

A primary interdependency exists with **WP3**, in particular **Task 3.1**, which focused on the review, specification, and conceptual design of fiber-optic sensing technologies for flood defence structures. Task 3.1 defined the sensing modalities, performance requirements, spatial resolution, installation principles, and post-processing needs based on relevant failure mechanisms in dikes and movable barriers. Deliverable D9.1 operationalises these specifications by implementing the proposed sensing concepts in laboratory-scale dikes and movable barrier elements at the Flood Proof Holland living lab and by experimentally evaluating their performance under controlled hydraulic and environmental loading conditions.

Task T9.1 is also closely linked to **WP4**, specifically **Task 4.4**, which addresses the modelling of failure and deterioration mechanisms of flood defences and their integration with in-situ monitoring data. The spatially distributed temperature and strain measurements acquired during the experiments documented in D9.1 provide experimental reference data for comparing measured structural responses with expected behaviour derived from numerical and surrogate models. This comparison supports the assessment of how fiber-optic sensing data can be used as inputs for model-based performance assessment and failure detection approaches.

A further interdependency exists with **WP10**, through **Task 10.4 and Deliverable D10.4**, which focus on the development of the monitoring software, data transmission system, and user interface for the Dutch demonstrator. The controlled experiments carried out at the Flood Proof Holland living lab and reported in D9.1 provide a suitable environment for testing the quality, continuity, and usability of post-processed fiber-optic sensor data required by the dashboard and real-time assessment tools developed in WP10. The results from D9.1 support the validation of data handling and integration workflows prior to demonstrator deployment.

Finally, Deliverable D9.1 establishes a forward interdependency with **WP11**, in particular **Deliverable D11.3**, which addresses the test and demonstration of the MULTICLIMACT framework across the Dutch demo sites. While demonstrator implementation is outside the scope of D9.1, the experimental validation under controlled conditions provides essential input for reducing technical risk and informing installation strategies, alert threshold definition, and operational procedures. The outcomes of D9.1 therefore contribute to ensuring that the monitoring system and associated tools can be effectively tested and demonstrated at territorial scale within WP11.

12. CONCLUSION

This deliverable presented the development, calibration, and preliminary validation of fiber optic-based monitoring systems for flood defence infrastructure within the MULTICLIMACT project, with a specific focus on earthen dikes and movable flood barriers. The work reported in D9.1 represents a critical transition from conceptual design to system readiness for real-world demonstration, addressing both sensing performance and deployment feasibility. This deliverable has advanced the development of fiber optic-based monitoring systems for flood defence infrastructure, delivering a technically validated and policy-relevant solution aligned with the objectives of the MULTICLIMACT project and the broader EU climate adaptation agenda. The work reported in D9.1 establishes a robust technical foundation for the deployment of distributed sensing technologies as operational tools for risk-informed flood defence management.

From a technical perspective, the deliverable demonstrates the feasibility of using distributed fiber optic sensing (DFOS) to monitor key physical processes governing the performance and failure mechanisms of both earthen dikes and movable flood barriers. For dikes, the successful recovery, mapping, and double-ended configuration of an existing buried fiber optic cable enabled high-quality Distributed Temperature Sensing (DTS) measurements over the full asset length. The integration of detailed field soil investigations with updated coupled hydro-thermal finite element modelling allowed the derivation of quantitative sensing requirements—measurement frequency, spatial resolution, and temperature accuracy—directly linked to moisture dynamics, pore pressure evolution, and effective stress changes in the vadose zone. These results confirm that the selected sensing architecture and interrogator technology are capable of resolving the fastest and most critical hydro-geotechnical processes relevant for stability assessment under extreme rainfall and drought conditions.

For movable flood barriers, the deliverable provides a technically sound strain-based monitoring concept grounded in linear elasticity theory and strain transfer mechanics. Through controlled laboratory and living-lab experiments, the system architecture—including fiber selection, Brillouin-based interrogation, calibration procedures, and mechanical clamp design—was iteratively optimized. The final clamp configuration demonstrates reliable strain transfer, mechanical robustness, and operational practicality, enabling the detection of load-induced deformation, joint behavior, and potential leakage pathways. These results confirm the suitability of distributed strain sensing as a scalable solution for modular and rapidly deployable flood protection systems.

From a policy and governance perspective, the outcomes of D9.1 directly support the transition from reactive flood defence management toward proactive, data-driven risk governance. Distributed fiber optic monitoring provides continuous, spatially dense information that significantly enhances observability of linear flood defence assets—structures that are traditionally monitored through sparse point measurements and periodic visual inspections. By enabling early detection of abnormal moisture gradients, thermal anomalies, and strain concentrations, the proposed systems support earlier intervention, reduce uncertainty during extreme events, and strengthen decision-making for emergency response, maintenance prioritization, and long-term investment planning.

The modelling-driven derivation of minimum system specifications is particularly relevant for policy uptake, as it links sensing performance to physically meaningful thresholds associated with failure mechanisms, rather than abstract sensor capabilities. This approach supports harmonisation with European standards for infrastructure safety, risk-based asset management, and resilience metrics, and facilitates integration with digital twins, early warning systems, and multi-hazard decision support platforms envisioned in EU climate adaptation strategies.

Furthermore, the solutions developed in this deliverable are inherently scalable and transferable. The same sensing principles, system architectures, and modelling frameworks can be applied to other linear infrastructure assets such as levees, embankments, canals, transport corridors, and pipelines. This scalability enhances the potential socio-economic impact by enabling wider adoption across regions, contributing to cost-effective climate adaptation and improved protection of citizens, critical services, and economic activities.

While the results presented are primarily based on controlled experiments and numerical simulations, the achieved level of technical maturity confirms readiness for full-scale deployment. Remaining challenges relate to long-term operational validation, automated data interpretation, and institutional integration within asset management workflows. These aspects will be addressed in the forthcoming demonstration phase of MULTICLIMACT, where continuous field monitoring will be used to validate performance under real operational and climatic conditions.

In conclusion, D9.1 delivers a technically robust, policy-relevant, and operationally viable fiber optic monitoring framework for flood defence infrastructure. The work contributes directly to Key Exploitable Result M#1, supporting evidence-based resilience planning, improved preparedness and response, and the long-term adaptation of flood defence systems to increasing climate variability and extreme events.

13. LITERATURE /REFERENCES

AB, COMSOL. 2019. “COMSOL Multiphysics® v. 5.4. Reference Manual.” COMSOL AB, Stockholm, Sweden., 1084.

Borek, Łukasz, Andrzej Bogdał, and Tomasz Kowalik. 2021. “Use of Pedotransfer Functions in the Rosetta Model to Determine Saturated Hydraulic Conductivity (Ks) of Arable Soils: A Case Study.” Land 10 (9): 959.

Boschert, Jeff, and Amster Howard. 2015. 2014 Updates to ASTM C12. August 18, 400–411. https://doi.org/10.1061/9780784479360.037.

Chui, Ting Fong May, and David L. Freyberg. 2009. “Implementing Hydrologic Boundary Conditions in a Multiphysics Model.” Journal of Hydrologic Engineering 14 (12): 1374–77. https://doi.org/10.1061/(ASCE)HE.1943-5584.0000113.

Danka, Jozsef, and LM Zhang. 2015. “Dike Failure Mechanisms and Breaching Parameters.” Journal of Geotechnical and Geoenvironmental Engineering 141 (9): 04015039.

Schaap, Marcel G., Feike J. Leij, and Martinus Th. van Genuchten. 2001. “Rosetta: A Computer Program for Estimating Soil Hydraulic Parameters with Hierarchical Pedotransfer Functions.” Journal of Hydrology 251 (3): 163–76. https://doi.org/10.1016/S0022-1694(01)00466-8.

Co-funded by
the European Union